

# h-Channels Contribute to Divergent Intrinsic Membrane Properties of Supragranular Pyramidal Neurons in Human versus Mouse Cerebral Cortex

## Highlights

- Ubiquitous *HCN1* expression in human, but not mouse, supragranular pyramidal neurons
- $I_h$  contributes substantially to human supragranular pyramidal neuron physiology
- Little contribution of  $I_h$  to mouse supragranular pyramidal neuron properties
- $I_h$  enhances theta band sensitivity of human supragranular pyramidal neurons

## Authors

Brian E. Kalmbach, Anatoly Buchin, Brian Long, ..., Costas A. Anastassiou, Ed S. Lein, Jonathan T. Ting

## Correspondence

briank@alleninstitute.org (B.E.K.),  
jonathant@alleninstitute.org (J.T.T.)

## In Brief

h-channel-related gene expression is more prominent in human than mouse supragranular cortex. Consequently, h-channels contribute to supragranular pyramidal neuron physiology more in human than mouse neocortex. These differences produce fundamental differences in synaptic integration in human supragranular pyramidal neurons.



# h-Channels Contribute to Divergent Intrinsic Membrane Properties of Supragranular Pyramidal Neurons in Human versus Mouse Cerebral Cortex

Brian E. Kalmbach,<sup>1,2,9,\*</sup> Anatoly Buchin,<sup>1</sup> Brian Long,<sup>1</sup> Jennie Close,<sup>1</sup> Anirban Nandi,<sup>1</sup> Jeremy A. Miller,<sup>1</sup> Trygve E. Bakken,<sup>1</sup> Rebecca D. Hodge,<sup>1</sup> Peter Chong,<sup>1</sup> Rebecca de Frates,<sup>1</sup> Kael Dai,<sup>1</sup> Zoe Maltzer,<sup>1</sup> Philip R. Nicovich,<sup>1</sup> C. Dirk Keene,<sup>3</sup> Daniel L. Silbergeld,<sup>4</sup> Ryder P. Gwinn,<sup>5</sup> Charles Cobbs,<sup>6</sup> Andrew L. Ko,<sup>4,7</sup> Jeffrey G. Ojemann,<sup>4,7</sup> Christof Koch,<sup>1</sup> Costas A. Anastassiou,<sup>1,8</sup> Ed S. Lein,<sup>1,4</sup> and Jonathan T. Ting<sup>1,\*</sup>

<sup>1</sup>Allen Institute for Brain Science, Seattle, WA 98109, USA

<sup>2</sup>Department of Physiology and Biophysics, University of Washington, Seattle, WA 98195, USA

<sup>3</sup>Department of Pathology, University of Washington School of Medicine, Seattle, WA 98195, USA

<sup>4</sup>Department of Neurological Surgery, University of Washington School of Medicine, Seattle, WA 98195, USA

<sup>5</sup>Epilepsy Surgery and Functional Neurosurgery, Swedish Neuroscience Institute, Seattle, WA 98122, USA

<sup>6</sup>The Ben and Catherine Ivy Center for Advanced Brain Tumor Treatment, Swedish Neuroscience Institute, Seattle, WA 98122, USA

<sup>7</sup>Regional Epilepsy Center at Harborview Medical Center, Seattle, WA 98104, USA

<sup>8</sup>Department of Neurology, University of British Columbia, Vancouver, BC V6T 1Z4, Canada

<sup>9</sup>Lead Contact

\*Correspondence: [briank@alleninstitute.org](mailto:briank@alleninstitute.org) (B.E.K.), [jonathant@alleninstitute.org](mailto:jonathant@alleninstitute.org) (J.T.T.)  
<https://doi.org/10.1016/j.neuron.2018.10.012>

## SUMMARY

Gene expression studies suggest that differential ion channel expression contributes to differences in rodent versus human neuronal physiology. We tested whether h-channels more prominently contribute to the physiological properties of human compared to mouse supragranular pyramidal neurons. Single-cell/nucleus RNA sequencing revealed ubiquitous *HCN1*-subunit expression in excitatory neurons in human, but not mouse, supragranular layers. Using patch-clamp recordings, we found stronger h-channel-related membrane properties in supragranular pyramidal neurons in human temporal cortex, compared to mouse supragranular pyramidal neurons in temporal association area. The magnitude of these differences depended upon cortical depth and was largest in pyramidal neurons in deep L3. Additionally, pharmacologically blocking h-channels produced a larger change in membrane properties in human compared to mouse neurons. Finally, using biophysical modeling, we provide evidence that h-channels promote the transfer of theta frequencies from dendrite-to-soma in human L3 pyramidal neurons. Thus, h-channels contribute to between-species differences in a fundamental neuronal property.

## INTRODUCTION

The development and gross anatomical organization of the mammalian cerebral cortex is stereotyped across species (Angevine and Sidman, 1961; DeFelipe, 2011; Rakic, 1974). However,

while all mammals possess a hexalaminar cortex comprising diverse neuronal cell types, the primate cortex has undergone dramatic evolutionary expansion, especially in layers 2 and 3 (L2 and L3) (DeFelipe, 2011). Consequently, in contrast to rodent, L2 and L3 in human neocortex are easily distinguishable from one another, and further sublaminar distinctions within L3 can be made based upon the size and organization of pyramidal neurons (DeFelipe, 2011; von Economo and Koskinas, 2007; Hill and Walsh, 2005; Molnár et al., 2014; Rakic, 2009). This evolutionary expansion and stratification suggests that there is functional specialization of neuronal properties within the supragranular layers of human neocortex.

Cross-species comparisons of supragranular pyramidal neuron properties indeed suggest that such neuronal specializations exist. For example, supragranular pyramidal neurons are larger and display more complex dendritic branching in the human compared to the mouse (Deitcher et al., 2017; Mohan et al., 2015). Additionally, there appear to be differences in the passive membrane properties of human neurons that may compensate for the filtering of electrical signals that would occur along such extensive dendritic arbors (Eyal et al., 2016). These differences may contribute to the unique cable properties of human pyramidal neuron dendrites and the enhanced ability of human neurons to track high-frequency synaptic input (Eyal et al., 2014; Testa-Silva et al., 2014).

While these differences in passive neuronal properties are notable, surprisingly little is known about how differential ion channel expression contributes to differences in active membrane properties between human versus rodent neurons. Voltage-gated ion channels shape a neuron's subthreshold integrative properties and endow it with the ability to generate nonlinear, regenerative events, including axonal action potentials and dendritic spikes (Bean, 2007; Johnston and Narayanan, 2008; Koch, 2004; Stuart and Spruston, 2015). In this way, ion channels are prime contributors to specialized neuronal function.



Intriguingly, large-scale cross-species comparisons of gene expression have revealed differences in the laminar expression of several ion channel-associated genes between mouse and human cortex (Zeng et al., 2012). Specifically, RNA for *HCN1*, a major pore-forming subunit of h-channels (Robinson and Siegelbaum, 2003), is differentially expressed in human versus mouse neocortex (Zeng et al., 2012). The hyperpolarization-activated non-specific cation current,  $I_h$ , which is carried by h-channels, greatly shapes a neuron's subthreshold integrative properties (Magee, 1998; Robinson and Siegelbaum, 2003; Williams and Stuart, 2000).

Here we use single-nucleus transcriptomics and *in vitro* slice physiology to provide evidence that h-channels contribute to the membrane properties of supragranular pyramidal neurons in human cortex more than in mouse cortex. We then use a biophysical model to provide insight into how the presence of h-channels affects the integrative properties of human supragranular pyramidal neurons. Our findings implicate a species-specific role for h-channels in dendritic integration of synaptic input that is most pronounced in deep L3 pyramidal neurons of human temporal cortex, which may generally represent an important evolutionary adaptation for very large pyramidal neurons in the human neocortex.

## RESULTS

To gain initial insight into whether human supragranular pyramidal neurons express h-channels, we utilized the existing online Allen Cell Types Database (<http://celltypes.brain-map.org>) consisting of single-nucleus RNA sequencing ( $n = 15,928$  nuclei from 8 donors) from human postmortem brain specimens with no prior history of neurological disorder. For comparison, in mouse, we analyzed a previously published single-cell RNA sequencing dataset obtained from mouse primary visual cortex (Tasic et al., 2016). We examined the expression levels of the genes encoding the four pore-forming subunits (*HCN1–HCN4*) of h-channels as well as *PEX5L*, which codes for a protein (TRIP8b) involved in modulating h-channel function and dendritic enrichment (Lewis et al., 2009; Robinson and Siegelbaum, 2003; Santoro et al., 2004).

In human temporal cortex, *HCN1* and *PEX5L* were prominently expressed in excitatory neurons in the supragranular and infragranular layers, whereas *HCN2–4* were much less abundant (Figure 1A). The average expression of *HCN1* was approximately equal (1.1-fold higher) in supragranular compared with infragranular excitatory neurons. In contrast, in the mouse neocortex, *Hcn1* and *Pex5l* were abundant in infragranular, but not supragranular, excitatory neurons (Figure 1B). The average expression of *Hcn1* was 3-fold higher in infragranular compared with supragranular excitatory neurons. Furthermore, *Hcn2–4* expression was relatively very low in excitatory neurons across the layers. Consistent with these observations, *HCN1* expression was observed in the supragranular and infragranular layers of human temporal cortex by *in situ* hybridization (ISH; Figure S1A; data obtained from the Allen Brain Atlas, <http://human.brain-map.org>). Furthermore, we observed substantial *HCN1* expression in supragranular excitatory neurons of human MTG (similar to infragranular excitatory neurons), especially those in deeper L3,

via multiplex fluorescence ISH (mFISH; Figure 1D). In contrast, in mouse, *Hcn1* expression was most conspicuous by ISH in layer 5 (L5) in multiple brain regions, including primary visual cortex and temporal association area (TeA; Figure S1B; data obtained from Allen Brain Atlas, <http://mouse.brain-map.org>). Using mFISH, we observed relatively low levels of *Hcn1* expression in supragranular compared with infragranular excitatory neurons of mouse TeA (Figures 1C). Notably, *HCN1* expression was relatively high in interneuron populations in mouse and human cortical tissue (Figures 1A and 1B; Figures S1C and S1D), suggesting that the scattered labeling in the supragranular layers of mouse cortex via ISH represent interneurons (Figure S1B). Together, these data suggest that there is widespread expression of h-channels, especially those containing HCN1 subunits, in human, but not mouse, supragranular pyramidal neurons.

### Physiological Evidence for Differences in $I_h$

To allow for direct between-species comparisons of pyramidal neuron membrane properties as a function of somatic distance from the pial surface, we first examined differences in the gross cytoarchitecture of mouse and human cortex. For these purposes, we chose the TeA of mouse cortex because it has been used in previous studies as a comparator for the middle temporal cortex typically resected from human epilepsy patients (Eyal et al., 2016; Mohan et al., 2015; Testa-Silva, 2010; Wang et al., 2015). In 350- $\mu$ m-thick DAPI-stained sections, we observed a sharp increase in cell density marking the boundary between L1 and L2 in both species (mouse  $n = 4$  slices from 4 mice,  $151 \pm 14 \mu\text{m}$ ; human  $n = 6$  slices from 6 patients,  $276 \pm 12 \mu\text{m}$  from pial surface). Below L2 was a sparser region of cells (L3) followed by a tight band of densely packed cells (L4, mouse  $470 \pm 6 \mu\text{m}$ , human  $1,469 \pm 34 \mu\text{m}$  from pial surface). Notably, the distance from the pial surface to the L3/L4 border ranged from 1,292–1,637  $\mu\text{m}$  in human sections and 453–508  $\mu\text{m}$  in mouse sections. L4 was followed by a decrease in cell density, marking L5 (mouse  $599 \pm 10 \mu\text{m}$  from pial surface, human  $1,736 \pm 37 \mu\text{m}$  from pial surface). Finally, the bottom of layer 6 (L6) was 2,963  $\pm 97 \mu\text{m}$  and 1,252  $\pm 29 \mu\text{m}$  from the pial surface in human and mouse neocortex, respectively. Thus, L2/3 represents ~40% and ~25% of the total thickness of human temporal gyrus and mouse TeA, respectively. These observations are consistent with previous reports that illustrate the large expansion of supragranular cortex in the human cortical column relative to mouse (DeFelipe, 2011; von Economo and Koskinas, 2007).

We performed whole-cell patch-clamp recordings from supragranular pyramidal neurons with cell bodies located throughout the entire depth of L2 and L3 (human  $n = 55$  cells from 10 patients, between 350 and 1,600  $\mu\text{m}$ ; mouse  $n = 39$  cells from 10 mice, between 162 and 465  $\mu\text{m}$  from the pial surface). Using IR-DIC optics, L3 was easily distinguishable from L4 in terms of both cell size and density; deep L3 consisted of sparse, large pyramidal neurons whereas L4 consisted of more densely packed granular-appearing cells. Morphological differences between mouse and human supragranular pyramidal neurons have been extensively detailed elsewhere; thus, we did not pursue this further (Deitcher et al., 2017; Mohan et al., 2015).

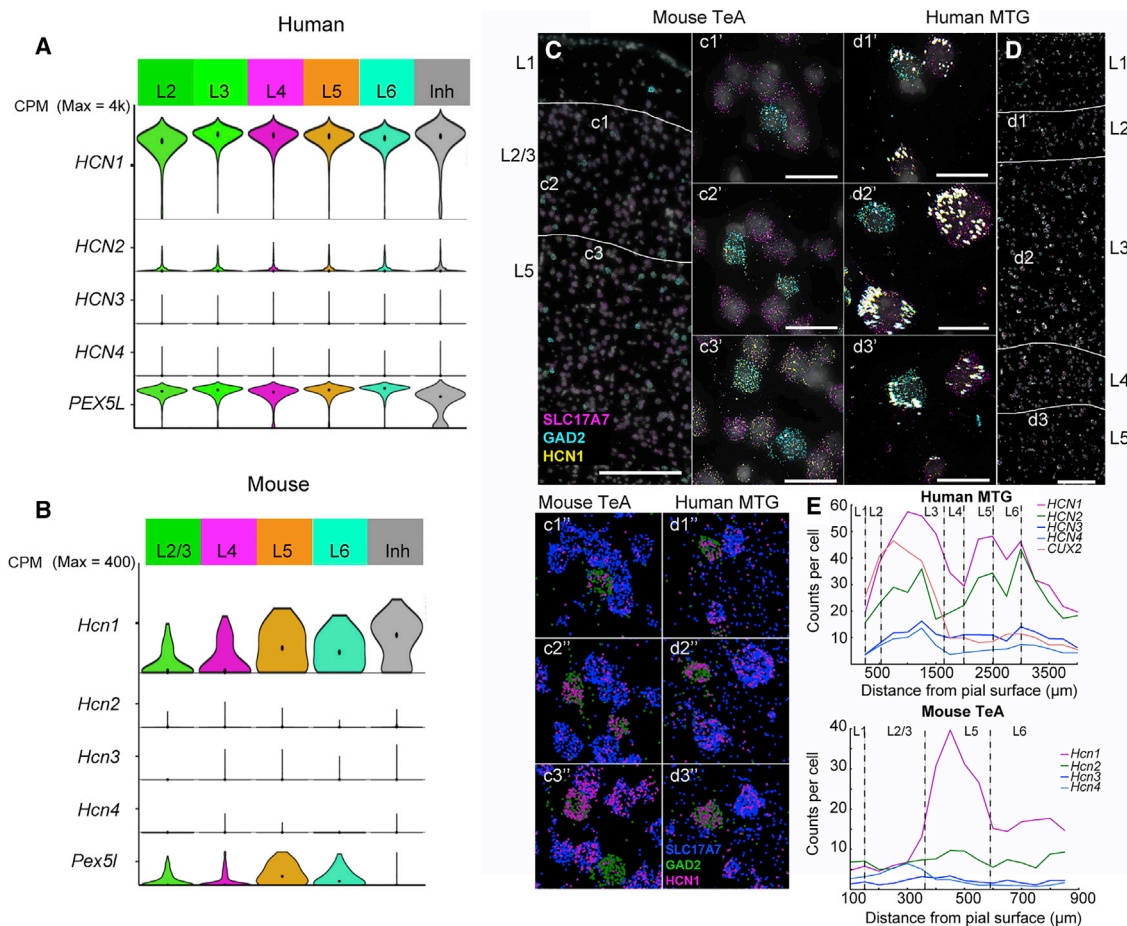


**Figure 1. HCN1-4 RNA Expression in Human versus Mouse Neocortex**

(A) Single-nucleus HCN channel subunit mRNA expression in excitatory neurons from human temporal cortex arranged by layer. Violin plots represent distribution of mRNA expression on a log scale with a maximum counts per million (CPM) of introns + exons value of 4,000. For reference, single-nucleus HCN channel subunit mRNA expression in inhibitory neurons, aggregated across all layers, is also shown.

(B–D) Single-cell HCN channel subunit mRNA expression in excitatory neurons from mouse visual cortex arranged by layer (B). The expression of *SLC17A7* (magenta), *GAD2* (turquoise), and *HCN1* (yellow) was assessed by mFISH in (C) mouse temporal association area (TeA), as well as (D) human middle temporal gyrus (MTG). In layers 2 and 3 of mouse TeA (c1, c1', c2, c2', c3, c3'), *Hcn1* expression in excitatory neurons is low compared with expression in L5 (c3, c3', c3''). *Hcn1* expression is high in *Gad2*-expressing inhibitory cells in all layers of mouse TeA (note, L4 is not prominent in mouse TeA). In human MTG, *HCN1* expression is prominent in excitatory and inhibitory neurons in the supragranular and infragranular layers (d1–d3''). Large white dots reflect fluorescence from lipofuscin. Images with '' are the same as images with ', but signals from each probe are color coded for clarity. Images in (C) and (D) are from composite images.

(E) RNA counts per cell as a function of depth from pial surface in human and mouse.

Scale bars in (C) and (D), 200  $\mu\text{m}$ . Scale bars in (c1'–d3''), 50  $\mu\text{m}$ .

We compared  $I_h$ -related membrane properties in human versus mouse pyramidal neurons. h-channels are open at relatively hyperpolarized potentials and thus contribute to a neuron's input resistance ( $R_N$ ) and resting membrane potential (RMP) (Magee, 1998; Robinson and Siegelbaum, 2003). In both mouse and human temporal cortex, we observed a positive correlation between RMP and somatic distance from the pial surface, such that the most depolarized neurons were found deep in L3 (mouse  $r^2 = 0.35$ ,  $p < 0.001$ ; human  $r^2 = 0.19$ ,  $p < 0.001$ ; Figures 2A–2E). In contrast, the  $R_N$  of mouse neurons increased as a function of somatic distance from pial surface ( $r^2 = 0.34$ ,  $p < 0.001$ ; Figures 2C and 2E), whereas the  $R_N$  of human neurons decreased ( $r^2 = 0.31$ ,  $p < 0.001$ ; Figures 2D

and 2E). Thus, in human temporal cortex, the neurons with the lowest input resistance were found deep in L3, whereas in mouse cortex they were found superficially, near the L1/2 border (Figure 2E). For human temporal cortex, these general observations were replicated in a subset of experiments in which  $R_N$  was measured at a common membrane potential of  $-65$  mV (Figure S2;  $n = 43$  from 10 patients,  $r^2 = 0.32$ ,  $p < 0.001$ ). In contrast, in mouse, there was no correlation between  $R_N$  and somatic distance from pia in a subset of experiments performed at  $-65$  mV (Figure S2;  $n = 24$  from 8 mice,  $r^2 = 0.02$ ,  $p = 0.53$ ), indicating that the depth dependence of  $R_N$  depends on RMP in mouse. Notably, the observation that  $R_N$  increases as a function of somatic depth from the pial

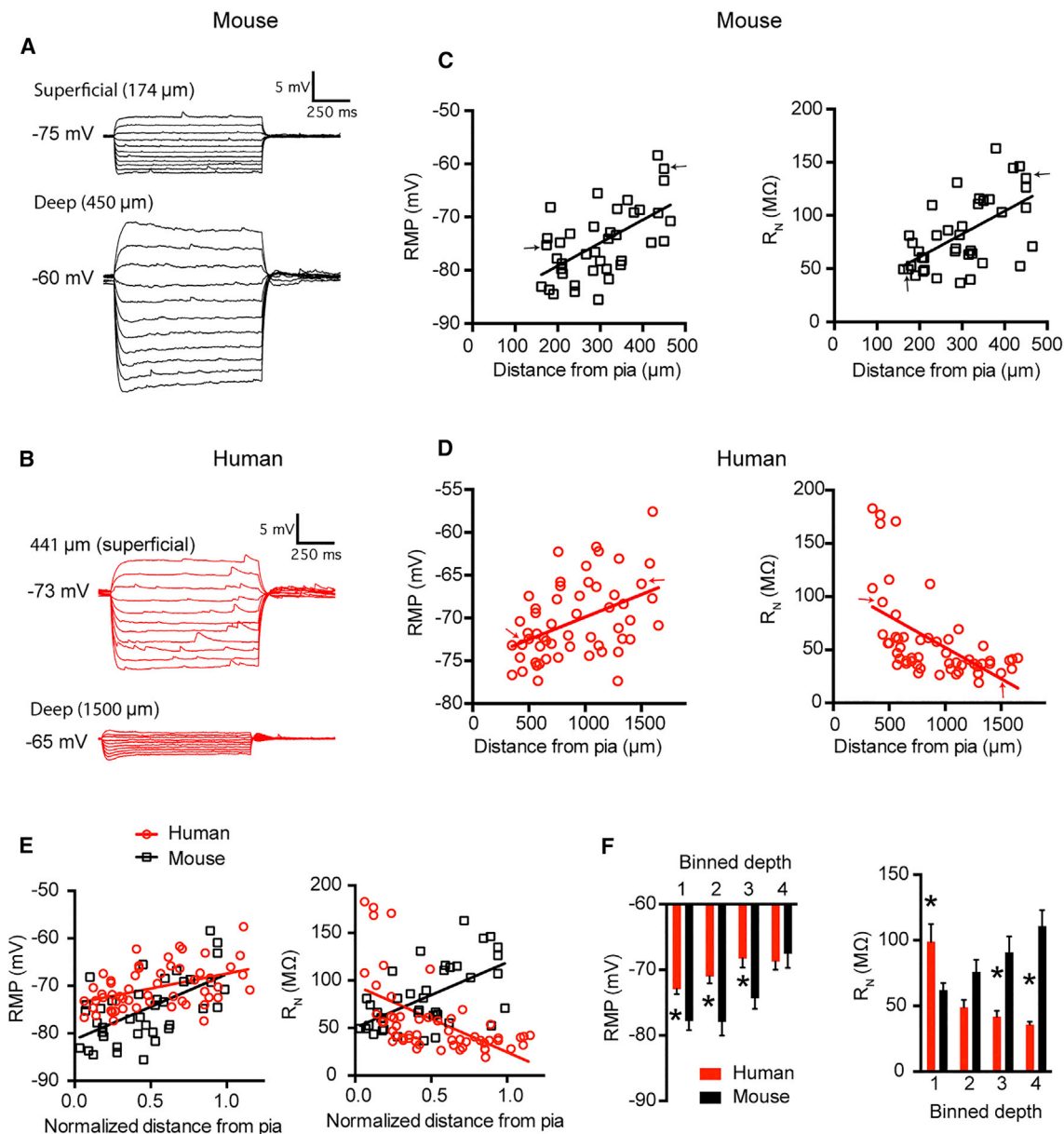


**Figure 2. Human and Mouse Supragranular Pyramidal Neurons Display Different Subthreshold Membrane Properties**

(A and B) Example voltage sweeps obtained from a superficial and deep supragranular pyramidal neuron in response to hyperpolarizing and depolarizing current injections in (A) mouse TeA and (B) human middle temporal gyrus.

(C) In mouse cortex, resting membrane potential and input resistance increase as a function of somatic distance from pia.

(D) In the supragranular layers of human middle temporal gyrus resting potential increases, but input resistance decreases as function of somatic distance from pia. Arrows correspond to sample voltage sweeps in (A) and (B).

(E) Resting potential and input resistance in mouse versus human cortex as a function of normalized somatic position in supragranular cortex.

(F) Data were binned into quarters based on the normalized distance of the soma from pia, where 1 is the most superficial quadrant and 4 is the deepest. Data are presented as mean  $\pm$  SEM. \* $p < 0.0125$ , mouse versus human post hoc t test with Bonferroni correction.

surface in mouse temporal association cortex is consistent with a previous report from mouse prefrontal cortex (Routh et al., 2017).

To make direct comparisons between mouse and human pyramidal neuron properties, we binned the data into quarters based on normalized soma distance from the pial surface to

the border of L3 and L4. Human neurons were more depolarized than mouse neurons throughout the first three-quarters of supragranular cortex ( $p = 0.03$ ; ANOVA followed by post hoc comparisons; Figure 2F). Furthermore, human neurons displayed a higher  $R_N$  in the most superficial portion of supragranular cortex and lower  $R_N$  in the lower half of supragranular cortex ( $p < 0.001$ ;

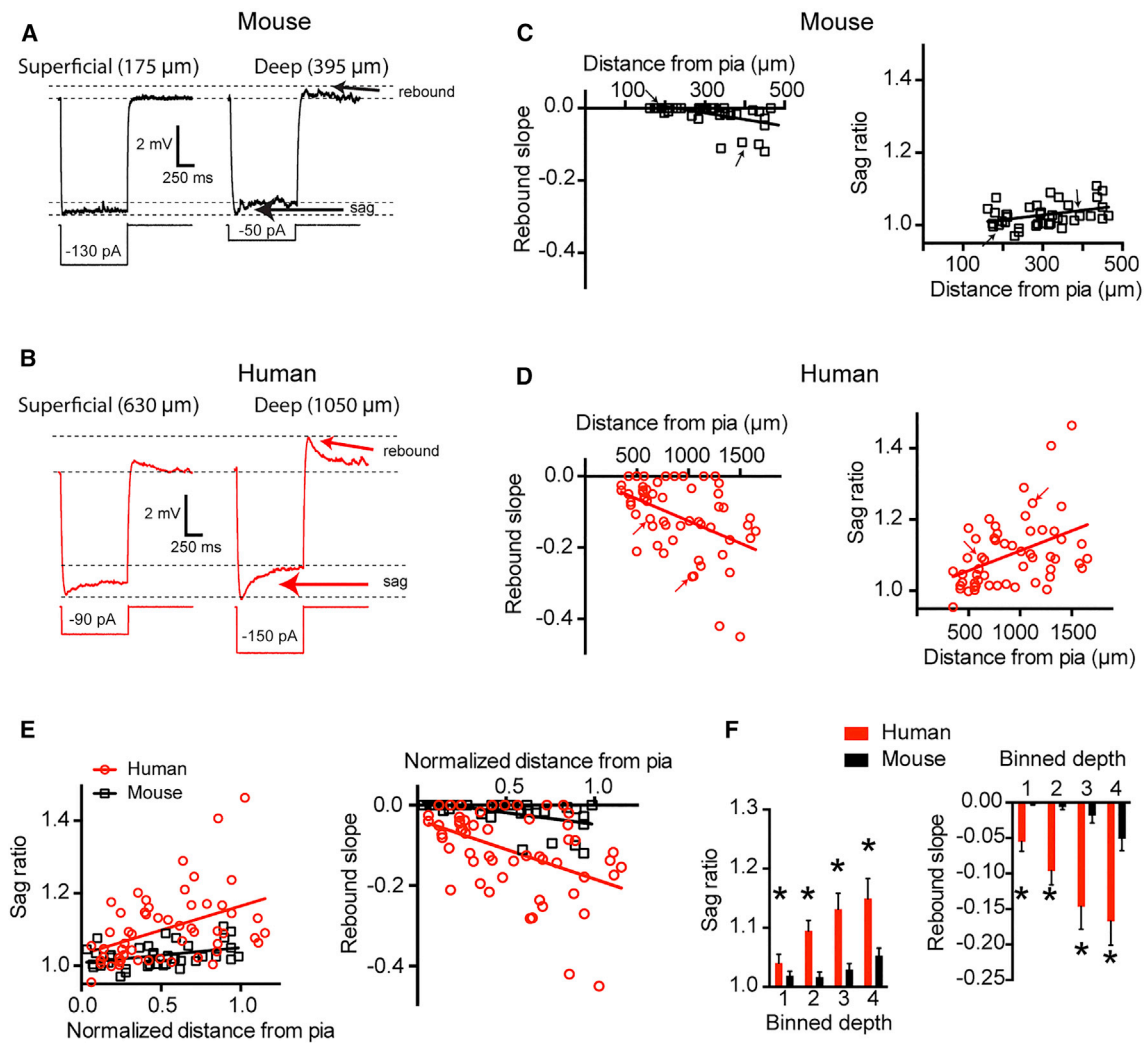


### Figure 3. $I_h$ -Related Membrane Properties are More Pronounced in Human Compared with Mouse Supragranular Pyramidal Neurons

(A and B) Example voltage sweeps were obtained from current injections that yielded  $\sim 6$  mV hyperpolarization in (A) mouse and (B) human supragranular pyramidal neurons. Arrows denote voltage sag and rebound potentials associated with  $I_h$ .

(C) Mouse neurons display little voltage sag or rebound in response to hyperpolarizing current injections.

(D) In contrast, rebound and sag were prominent in human supragranular cortex, especially in deep L3. Arrows correspond to sample voltage sweeps in (A) and (B).

(E) Sag and rebound in mouse and human cortex as a function of normalized somatic position in supragranular cortex.

(F) Data binned into quadrants and presented as mean  $\pm$  SEM. \* $p < 0.001$  mixed factor ANOVA effect of species.

ANOVA followed by post hoc comparisons; Figure 2F). Thus, there are significant distance-dependent differences in the properties of human versus mouse supragranular pyramidal neurons.

In addition to  $R_N$  and RMP,  $I_h$  contributes to several unique membrane properties. Specifically,  $I_h$  is associated with a characteristic voltage “sag” upon membrane hyperpolarization and a rebound potential upon release from hyperpolarization (Figures 3A and 3B; Robinson and Siegelbaum, 2003). While in the supragranular layers of mouse TeA these  $I_h$ -related membrane properties were largely absent, we did observe a few neurons deep in L3 that displayed modest amounts of sag and rebound (sag  $r^2 = 0.14$ ,  $p = 0.02$ ; rebound  $r^2 = 0.26$ ,  $p < 0.001$ ; Figure 3C). In contrast, sag and rebound were apparent in many human pyrami-

dal neurons throughout the supragranular layers and were positively correlated with somatic depth from the pial surface (sag  $r^2 = 0.18$ ,  $p = 0.001$ ; rebound  $r^2 = 0.20$ ,  $p < 0.001$ ; Figure 3D). These response properties are plotted as a function of normalized depth from pia to the border of L3 and L4 and illustrate the marked differences in  $I_h$ -related properties between mouse and human supragranular pyramidal neurons (Figure 3E). These general observations were replicated in a subset of experiments performed at  $-65$  mV (Figure S2; mouse  $n = 24$  from 8 mice, sag  $r^2 = 0.01$ ,  $p = 0.65$ , rebound  $r^2 = 0.35$ ,  $p = 0.002$ ; human  $n = 43$ , sag  $r^2 = 0.14$ ,  $p = 0.01$ , rebound  $r^2 = 0.22$ ,  $p < 0.001$ ). Finally, direct between-species comparisons revealed that human neurons possessed more sag and rebound at all levels of supragranular

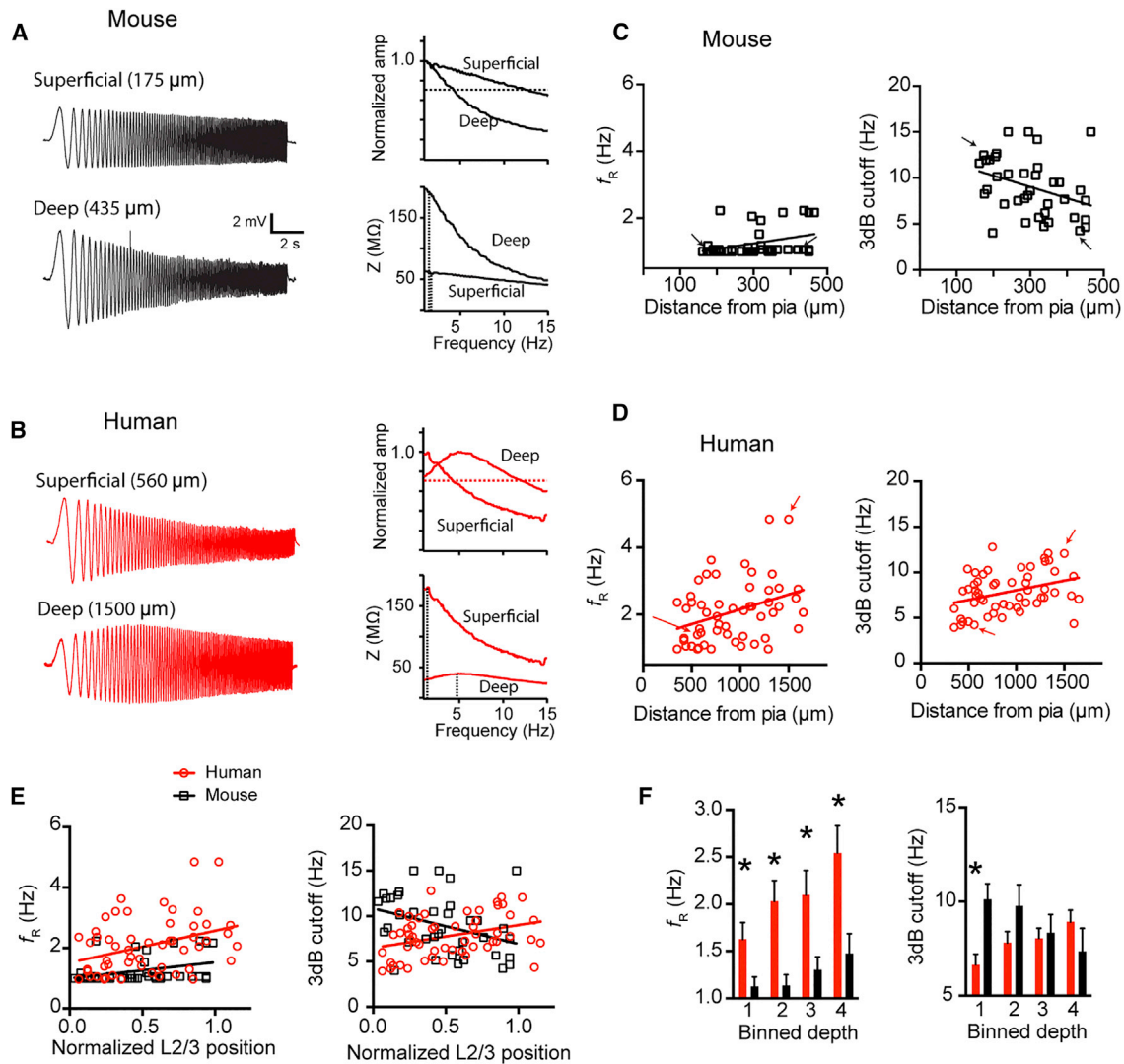


**Figure 4. Mouse and Human Supragranular Pyramidal Neurons Display Different Subthreshold Filtering Properties**

(A and B) Example voltage responses to a chirp stimulus current injection in a superficial and deep supragranular pyramidal neuron in (A) mouse and (B) human cortex. Impedance amplitude profile (ZAP) and normalized frequency response curves are also shown for these example neurons. Dotted lines mark the resonant frequency in the ZAP and the 3 dB cutoff in the normalized frequency response curves.

(C) Mouse neurons were largely non-resonant and became more low pass as a function of somatic depth from pia.

(D) Resonant frequency correlated with somatic depth from pia in human cortex. Additionally, in human cortex, 3 dB cutoff frequency was correlated with somatic depth from pia. Arrows correspond to sample voltage sweeps in (A) and (B).

(E) Resonant frequency and 3 dB cutoff as a function of normalized depth from pia in mouse and human supragranular cortex.

(F) Data binned into quadrants and presented as mean  $\pm$  SEM. For binned resonant frequency data \* $p < 0.001$  mixed factor ANOVA effect of species. For binned 3 dB cutoff data, \* $p < 0.0125$ , mouse versus human post hoc *t* test with Bonferroni correction.

cortex compared to their mouse counterparts (Figure 3F;  $p < 0.001$ ; ANOVA followed by post hoc comparisons).

The slow activation and deactivation kinetics of h-channels contribute greatly to the filtering properties of a neuron. Specifically,  $I_h$  contributes to membrane resonance in the  $\sim 2$ –7 Hz range (Dembrow et al., 2010; Hutcheon et al., 1996; Kalmbach et al., 2013; 2017; 2015; Narayanan and Johnston, 2007; Nolan et al., 2004; Ulrich, 2002). To test for differences in the subthreshold filtering properties of human versus mouse pyramidal neurons, we measured the response of pyramidal neurons

throughout the depth of supragranular cortex to a chirp stimulus. In addition to measuring the resonant frequency of neurons, we also calculated the 3 dB cutoff as a way to quantify differences in low-pass filtering. Mouse pyramidal neurons were largely non-resonant at either RMP or  $-65$  mV, although there were a few neurons located deep in L3 that showed modest resonance (Figures 4A and 4C; Figure S2;  $r^2 = 0.13$ ,  $p = 0.02$ ;  $-65$  mV  $r^2 = 0.01$ ,  $p = 0.59$ ). Additionally, the 3 dB cutoff of mouse neurons was negatively correlated with somatic depth from pia at RMP (Figure 4C,  $r^2 = 0.12$ ,  $p = 0.03$ ), but not at  $-65$  mV (Figure S2;

$r^2 = 0.01$ ,  $p = 0.99$ ), indicating that the filtering properties of deep supragranular pyramidal neurons were more low-pass than superficial ones at RMP. In contrast, many human pyramidal neurons displayed membrane resonance in the  $\sim 2$ –5 Hz range. Indeed, resonance was positively correlated with somatic depth from pia in human supragranular cortex when measured from RMP (Figure 4A and D;  $r^2 = 0.13$ ,  $p = 0.007$ ) and  $-65$  mV (Figure S2;  $r^2 = 0.32$ ,  $p < 0.001$ ). In contrast to mouse pyramidal neurons, the 3 dB cutoff of human pyramidal neurons was positively correlated with somatic depth from the pial surface (Figure 4D; RMP,  $r^2 = 0.12$ ,  $p = 0.01$ ; Figure S2;  $-65$  mV  $r^2 = 0.22$ ,  $p = 0.001$ ). The 3 dB cutoff and resonance frequency of mouse and human pyramidal neurons are also plotted as a function of normalized soma position in L2/3 (Figure 4E). Direct comparisons revealed that human neurons had a higher resonant frequency than mouse neurons at all relative distances from the pial surface (Figure 4F;  $p < 0.001$ ; ANOVA). Furthermore, the most superficial human neurons had a lower 3 dB cutoff than mouse neurons (Figure 4F;  $p = 0.01$ ; ANOVA followed by post hoc t test). These data highlight striking differences in the subthreshold filtering properties of mouse versus human L2/3 pyramidal neurons, further supporting the hypothesis that  $I_h$  is prominent in human, but not in mouse, supragranular pyramidal neurons.

In addition to contributing to subthreshold properties,  $I_h$  impacts the action potential output of a neuron in response to suprathreshold current injections (Fan et al., 2005; Gu et al., 2005). Specifically, differences in the number of action potentials elicited by a given current injection can reflect differences in  $I_h$ . Thus, we also tested for between-species differences in the response of individual pyramidal neurons to 1 s, depolarizing direct current injections (250, 500, and 750 pA). In mouse TeA, excitability (here defined as the number of spikes in response to a given current injection) was positively correlated with soma distance from the pial surface (Figure 5A; 250 pA  $r^2 = 0.38$ ,  $p < 0.001$ , 500 pA  $r^2 = 0.17$ ,  $p = 0.01$ , 750 pA  $r^2 = 0.12$ ,  $p < 0.03$ ), such that the most excitable neurons were located deep in L3. In contrast to mouse cortex, excitability was negatively correlated with somatic distance from the pial surface in human cortex such that the most excitable neurons were located superficially (Figure 5B; 250 pA  $r^2 = 0.21$ ,  $p < 0.001$ , 500 pA  $r^2 = 0.44$ ,  $p < 0.001$ , 750 pA  $r^2 = 0.47$ ,  $p < 0.001$ ). Figure 5C plots the action potential frequency in response to three different amplitudes of current injection in mouse versus human temporal cortex normalized for the position of the recorded neuron through the depth of L2/3. Direct comparisons also revealed several depth-dependent differences in excitability between mouse and human pyramidal neurons (Figure 5D; ANOVA,  $p < 0.001$  followed by post hoc t tests). These general observations were replicated in a subset of experiments when the membrane potential was held at a common level via direct current injection ( $-65$  mV, Figure S2). These data suggest that the depth-dependent intrinsic excitability of mouse and human pyramidal neurons differs dramatically. While these results mirror the depth-dependent differences in  $I_h$ -dependent membrane properties described above, there are likely many contributors to these differences in excitability.

The data presented thus far were collected from tissue obtained from patients with temporal lobe epilepsy. To assess the generality of the between-species differences in  $I_h$ -related membrane properties, we also obtained data from temporal cortex (three patients) and frontal cortex (two patients) tissue from patients diagnosed with a deep brain tumor. The depth-dependent  $I_h$ -related membrane properties observed in tissue obtained from epilepsy patients were also observed in supragranular cortex from tumor patients (Figure S3). While there were subtle differences in  $I_h$ -related membrane properties of neurons recorded from tumor versus epilepsy patients (e.g., neurons recorded from tumor patients tended to have slightly more sag than those recorded from epilepsy patients), these differences did not depend upon somatic distance from the pial surface. Indeed, the dependence of  $I_h$ -related features on somatic distance from the pial surface was indistinguishable for neurons recorded from tumor versus epilepsy patients (Figure S3). These observations suggest that  $I_h$ -related membrane properties in supragranular pyramidal neurons are not solely related to disease state. Consistent with this conclusion, robust h-channel-related RNA expression was observed in supragranular excitatory neurons in brain tissue obtained from donors with no previous history of seizures or tumors (Figure 1A; Figure S1A).

Finally, we tested whether other factors might contribute to the  $I_h$ -related features we observed in human temporal cortex. Cells from different patients were sampled from similar cortical depths, and the distribution of data points were similar across patients with the exception of one patient. However, the distance-dependent differences in  $I_h$ -related properties were robustly observed regardless of inclusion or exclusion of the data from this patient (Figure S4). Similarly, prominent  $I_h$ -related membrane properties were observed across a wide range of patient ages and seizure histories (Figure S5). The age independence of  $I_h$ -related properties is consistent with observations that *HCN1* RNA expression stabilizes by childhood (Colantuoni et al., 2011; Figure S5). Nonetheless, we cannot rule out subtle contributions of age to supragranular pyramidal neuron physiology not detected here.

### Pharmacological Evidence for $I_h$ in Human Supragranular Pyramidal Neurons

To test for the relative contribution of  $I_h$  to the intrinsic membrane properties of human versus mouse pyramidal neurons, we bath applied the h-channel blocker ZD7288 while monitoring resting membrane potential (Figure 6). For these experiments, we focused on recording from neurons located deeper in supragranular cortex, where  $I_h$ -related properties were more apparent in both species. On average, ZD7288 hyperpolarized the RMP by  $8.15 \pm 1.52$  mV in human neurons and  $0.59 \pm 0.97$  mV in mouse neurons (Figure 6A). In addition,  $R_N$ , when measured at a common potential of  $-65$  mV increased by  $60.43\% \pm 9.94\%$  in human neurons (from  $48.92 \pm 4.54$  M $\Omega$  to  $76.39 \pm 6.47$  M $\Omega$ ) and by  $13.27\% \pm 4.73\%$  in mouse neurons (from  $136.61 \pm 4.27$  M $\Omega$  to  $155.91 \pm 7.86$  M $\Omega$ ; Figure 6B). ZD7288 also eliminated voltage sag, rebound, and resonance, indicating that these membrane properties are dependent on functional h-channels in human supragranular pyramidal neurons (Figure S6). In addition,

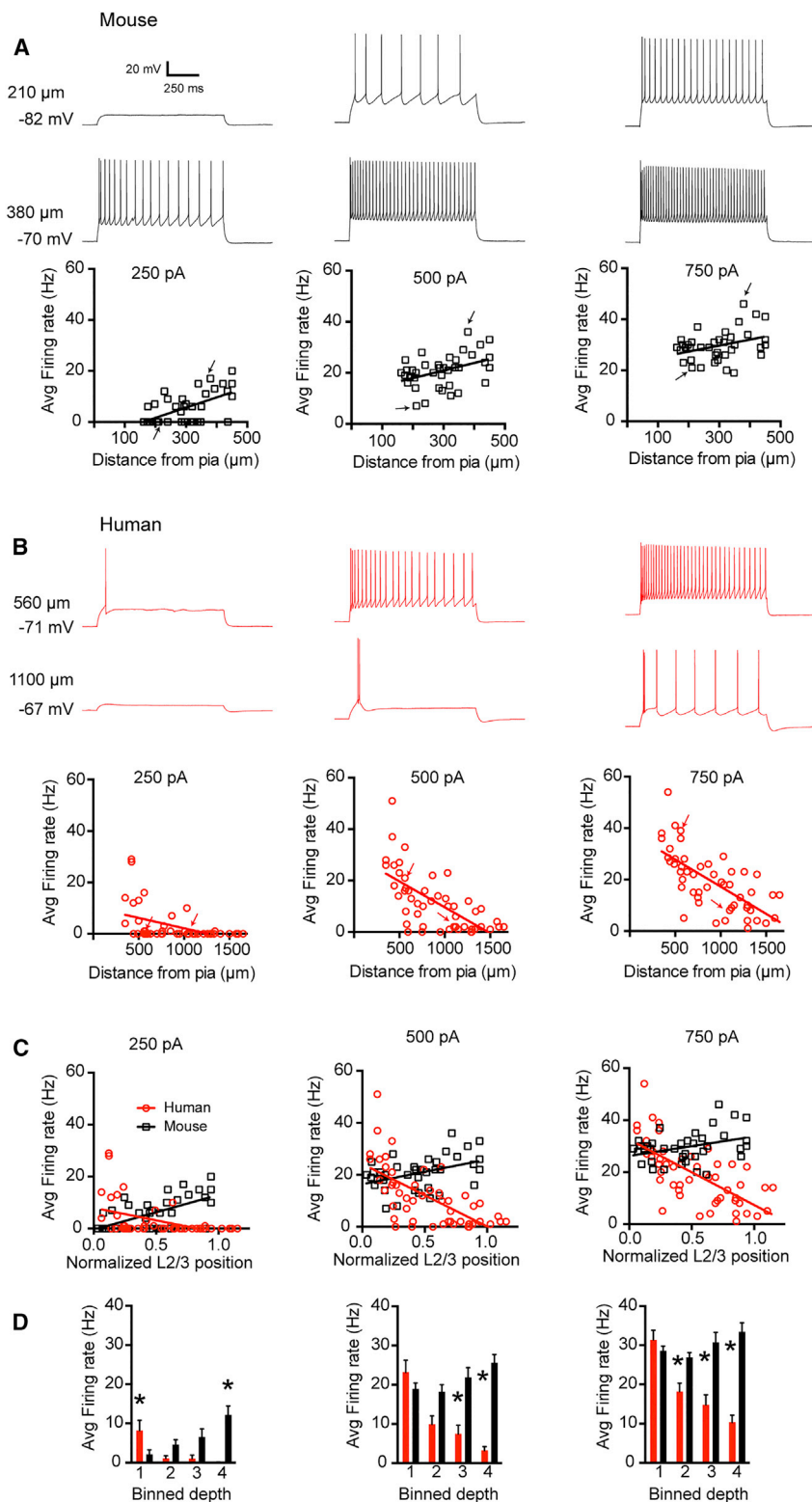


**Figure 5. Excitability of Mouse versus Human Pyramidal Neurons as a Function of Somatic Distance from Pia**

(A) The number of APs elicited by a given current injection increased as a function of somatic depth from pia in supragranular mouse cortex. Example sweeps obtained from a superficial and deep neuron in response to 250, 500, and 750 pA are shown.

(B) The number of APs elicited by a given current injection decreased as a function of somatic depth from pia in supragranular human cortex. Example sweeps obtained from a superficial and deep neuron in response to 250, 500, and 750 pA are shown. Arrows correspond to sample voltage sweeps in (A) and (B).

(C) Average firing rate as a function of normalized position within supragranular cortex in mouse versus human.

(D) Data binned into quadrants and presented as mean  $\pm$  SEM. \* $p < 0.0125$  mouse versus human post hoc *t* test with Bonferroni correction.

the average input/output curve in Figure 6C. Together, these data suggest that  $I_h$  contributes to the intrinsic membrane properties of human supragranular pyramidal neurons significantly more than mouse neurons.

Finally, we also tested the effect of ZD7288 on superficial human neurons to assay whether blocking h-channels eliminates the depth-dependent properties we observe in human supragranular cortex. The effect of ZD7288 on  $R_N$ , RMP, and action potential generation depended upon the depth of the soma from the pial surface, with the largest changes occurring deeper in the supragranular layers (Figure S6). Furthermore, blocking h-channels did not eliminate the depth dependence of  $R_N$  or excitability (Figure S6). Thus, although h-channels contribute to the depth-dependent differences in  $R_N$  and excitability we observe, clearly other factors contribute.

### Impact of $I_h$ on Subthreshold Integration in Human Neurons

What influence might  $I_h$  have on the input and output properties of human supragranular pyramidal neurons? While  $I_h$  affects many aspects of neuronal function, perhaps its most consistently observed influence is on subthreshold synaptic integration. h-channel expression in many neurons counteracts the distance-dependent capacitive filtering of synaptic input as it propagates from

dendrite to soma (Dembrow et al., 2015; Harnett et al., 2015; Koch et al., 1990; Magee, 1999; Rall, 1967; Stuart and Spruston, 1998; Vaidya and Johnston, 2013; Williams and Stuart, 2000);

ZD7288 reduced the cutoff frequency of human neurons more so than mouse (Figure S6). ZD7288 also increased the excitability of human pyramidal neurons, as is apparent in the parallel shift of

dendrite to soma (Dembrow et al., 2015; Harnett et al., 2015; Koch et al., 1990; Magee, 1999; Rall, 1967; Stuart and Spruston, 1998; Vaidya and Johnston, 2013; Williams and Stuart, 2000);

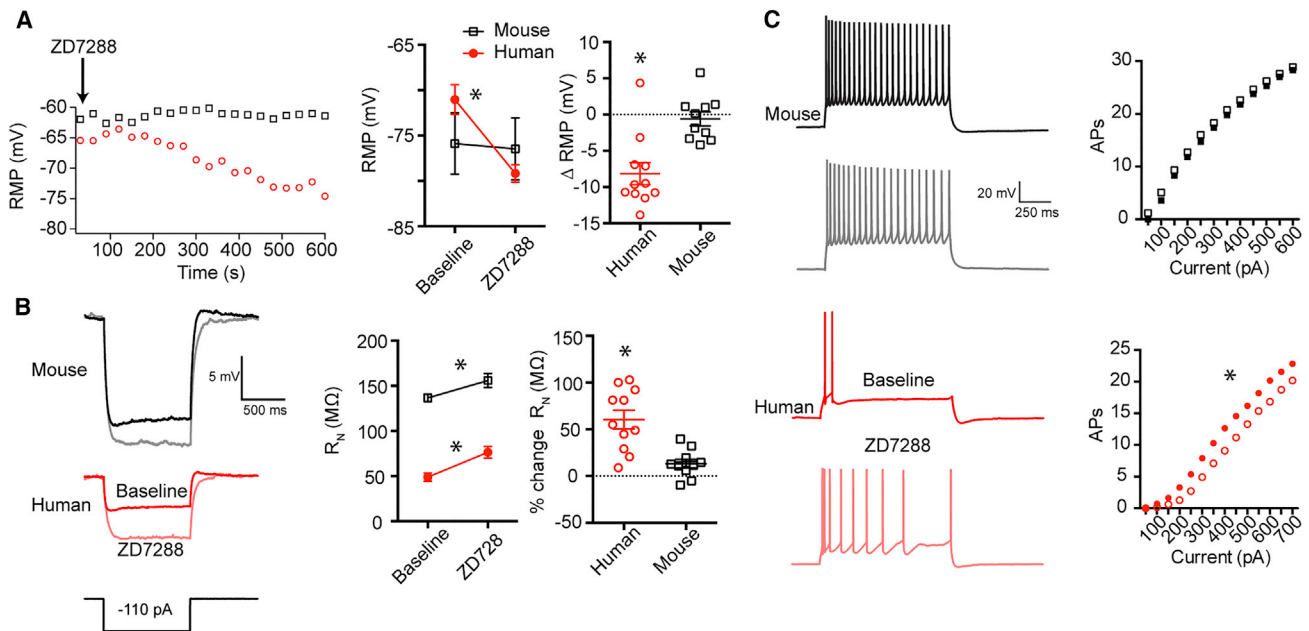


**Figure 6. Pharmacological Evidence for  $I_h$  in Human Supragranular Pyramidal Neurons**

(A) Bath application of  $10 \mu\text{M}$  ZD7288 hyperpolarized human neurons by  $\sim 8 \text{ mV}$  ( $p < 0.001$ , Bonferroni's post hoc comparison), but no consistent change in mouse neurons was observed ( $p = 0.56$ , Bonferroni's post hoc comparison). The plot at the left shows RMP as a function of time for two example recordings.

(B)  $10 \mu\text{M}$  ZD7288 produced an increase in input resistance in human and mouse supragranular pyramidal neurons ( $p < 0.001$ , Mixed-ANOVA effect of ZD7288). The percent change in input resistance was larger in human compared with mouse ( $p < 0.001$ ,  $t$  test). Example voltage responses to hyperpolarizing current injections are shown to the left.

(C)  $10 \mu\text{M}$  ZD7288 increased the excitability of human ( $p < 0.001$ , RM ANOVA), but not mouse, pyramidal neurons ( $p = 0.13$ , RM ANOVA). Plots are averages from 11 human neurons from 4 patients and 10 mouse neurons from 6 animals. Data are presented as mean  $\pm$  SEM.

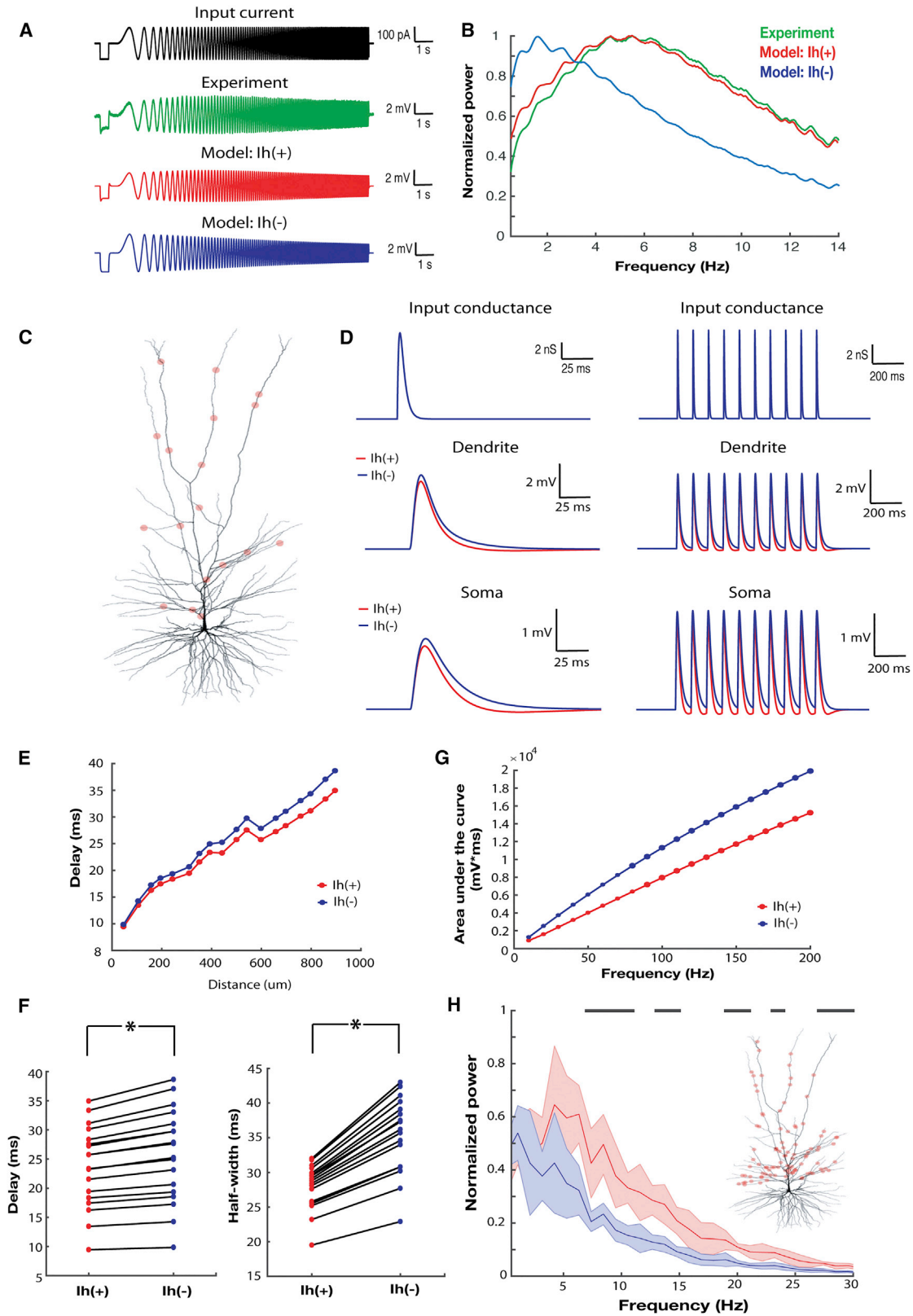
this ensures that the kinetics of synaptic potentials at the soma are relatively independent of synaptic origin. Additionally,  $I_h$  narrows the window for temporal integration of synaptic input often to synaptic inputs with frequency components in the theta (4–12 Hz) band (Das and Narayanan, 2014; Dembrow et al., 2015; Kalmbach et al., 2017; Narayanan and Johnston, 2008; 2007; Ulrich, 2002; Vaidya and Johnston, 2013). To explore whether  $I_h$  might similarly affect the integrative properties of human supragranular pyramidal neurons, we used a morphologically precise computational model of a human L3 pyramidal neuron that possessed no active conductances other than  $I_h$ .

We first asked whether the presence of  $I_h$  in the model reproduced the subthreshold resonance observed in many deep supragranular pyramidal neurons in human temporal cortex (Figures 7A and 7B). The presence of  $I_h$  significantly affected the response of the model to a somatic chirp stimulus. Notably, even though the chirp stimulus was not used to generate the computational model, in the presence of  $I_h$  (model:  $I_h (+)$ ) the model displayed band-pass filtering properties closely resembling those observed experimentally (Figures 7A and 7B). In contrast, in the absence of  $I_h$  (model:  $I_h (-)$ ), the frequency response of the model markedly departed from the experimentally measured one (Figures 7A and 7B).

We next assessed how the presence of  $I_h$  in the model affected the integration of synaptic input arriving at various locations along the dendrite. To this end, we activated AMPA-like conductances at several locations along the dendritic arbor and

measured the resultant local dendritic and propagated somatic voltage responses (Figures 7C and 7D). In a totally passive neuron, low-pass filtering severely attenuates and distorts synaptic inputs as they propagate to the soma, especially those arriving at distal locations (Koch, 2004; Koch et al., 1990; Rall, 1967; Stuart and Spruston, 1998). To quantify the effect of  $I_h$  on single excitatory postsynaptic potential (EPSP) kinetics, we measured the delay in the peak of the somatic EPSP relative to the peak of the local dendritic EPSP as well as the half-width of the somatic EPSP. In the passive model ( $I_h (-)$ ), a distance-dependent increase in the delay of the somatic EPSP relative to the dendritic synaptic conductance was observed as well as in the half-width of the somatic EPSP. In contrast, in the  $I_h (+)$  model, the delay between the peak of the dendritic and somatic EPSPs was significantly reduced, especially at distal locations as was the half-width of the somatic EPSP (Figures 7E and 7F). Thus, the inclusion of  $I_h$  produced EPSPs at the soma of the model L3 human pyramidal neuron with a significantly faster time course.

These effects suggest that  $I_h$  influences the temporal summation of synaptic input in human supragranular pyramidal neurons; faster EPSP kinetics modestly reduce the temporal window wherein inputs can summate (Dembrow et al., 2015; Magee, 1999; Vaidya and Johnston, 2013; Williams and Stuart, 2000). To examine this possibility, we initiated bursts of AMPA-like conductances at various frequencies and locations along the dendrite and measured the resulting somatic response. The total



(legend on next page)

somatic depolarization (i.e., the integral of the somatic voltage response) was reduced across several frequencies of synaptic input (Figure 7G). Thus, the presence of  $I_h$  in the model L3 human pyramidal neuron reduced the temporal summation of synaptic inputs.

Finally, by opposing changes to membrane potential,  $I_h$  can impart phenomenological inductance to the membrane. This has the effect of counteracting lags in the phase of membrane potential relative to current that is imposed by capacitive elements of the membrane (Koch, 1984; Mauro, 1961). This inductive property of  $I_h$  is also known to promote the transfer to the soma of synaptic input containing of theta frequencies (Dem-brow et al., 2015; Narayanan and Johnston, 2008; Ulrich, 2002; Vaidya and Johnston, 2013). To test whether  $I_h$  also promotes the selective transfer of frequencies in the theta frequency range in human supragranular pyramidal neurons, we initiated AMPA-like synaptic input with a Poisson process (4 Hz) at 1,000 locations along the dendritic arbor (Figure 7H, inset). Comparing the  $I_h(+)$  and  $I_h(-)$  models revealed that the presence of  $I_h$  resulted in an increase in power in the 5–15 Hz range of the somatic voltage response (Figure 7H). Importantly, this enhancement of theta band frequencies did not depend upon the somatic-dendritic gradient of  $I_h$  used in the model (Figure S7). These results were also observed when passive membrane properties were equal in each compartment of the model (Figure S7). Thus, although the dendrite was presented with a random spatial-temporal pattern of input, frequencies in the 5–15 Hz range were preferably passed to the soma in the  $I_h(+)$  model. The high-pass filtering properties of  $I_h$ , together with the low-pass filtering properties of the passive dendritic membrane, impart the band-pass shape of this transfer function (Hutcheon and Yarom, 2000).

## DISCUSSION

We have provided new evidence indicating a disparate contribution of h-channels to human versus mouse supragranular pyramidal neuron properties. Previous studies have largely focused on differences in the morphological, synaptic, and/or passive membrane properties of rodent versus human supragranular pyramidal neurons. For example, human neurons are larger and possess a more complex dendritic arbor compared with mouse (Deitcher et al., 2017; Mohan et al., 2015). Differences in dendritic morphology and passive dendritic membrane prop-

erties could contribute to differences in the cable properties of human versus rodent pyramidal neurons (Eyal et al., 2016). Likewise, these differences, together with differences in synaptic properties may contribute to the reported high-bandwidth processing capabilities of human neurons (Eyal et al., 2014; Testa-Silva et al., 2014). Our observation of cortical depth-dependent differences in mouse versus human pyramidal neuron properties adds to this growing list of interspecies disparities in cortical pyramidal neuron properties. Intriguingly, the depth-dependent differences in intrinsic properties we observe in human cortex parallel the lamination and differentiation of cell size that occurs along the radial axis of the supragranular layers (von Economo and Koskinas, 2007; Hill and Walsh, 2005; Molnár et al., 2014; Rakic, 2009). As such, the depth dependence of these membrane properties may reflect an evolutionary adaptation for the expanded supragranular cortex of humans.

Our findings contrast with a previous report that found few correlations between L2/3 membrane properties and somatic depth from the pial surface in human cortex (Deitcher et al., 2017). This discrepancy may be due to differences in sampling. The dataset included in the previous report was smaller than the current set. Thus, it is possible that our dataset captured more depth-dependent variability in intrinsic properties simply because of increased sampling. Relatedly, we sampled a wider range of somatic depths from the pial surface than the previous study. Thus, the previous study may not have sampled the most superficial of L2 or the deepest portions of L3, where the largest differences in intrinsic membrane properties exist.

To our knowledge, our findings are the first to directly implicate a particular ion channel in differences between human and rodent pyramidal neuron properties. Supragranular pyramidal neurons in rodent cortex express little h-channel-related protein or RNA (Figure 1) (Lőrincz et al., 2002; Santoro et al., 2000; Zeng et al., 2012). Furthermore, mouse and rat supragranular pyramidal neurons display very few hallmarks of  $I_h$  across several areas of cortex (Larkum et al., 2007; Routh et al., 2017; van Aerde and Feldmeyer, 2015). Together, these observations suggest that  $I_h$  contributes very little to rodent supragranular pyramidal neuron physiology regardless of cortical region. In contrast, human supragranular pyramidal neurons display prominent voltage sag (Deitcher et al., 2017; Foehring and Waters, 1991), which we show here depends on h-channels. Furthermore, sag and other  $I_h$ -related properties in human cortex are more prominent in deep, compared to superficial, L2/3 pyramidal neurons

### Figure 7. $I_h$ Affects the Subthreshold Integrative Properties of a Morphologically Precise Human L3 Pyramidal Neuron Model

- (A) Voltage response elicited by somatic chirp stimulus of a L3 pyramidal neuron (green), biophysical model with  $I_h$  (red), and biophysical model without  $I_h$ .  
 (B) Power spectrum of somatic membrane potential response to chirp stimulus shown in (A) (blue: experiment; green:  $I_h(+)$  model; red:  $I_h(-)$  model).  
 (C) Morphological reconstruction of a human L3 pyramidal neuron used for the simulations.  
 (D) Single (left) or bursts (right) of AMPA-like conductances were injected at single synaptic locations (top), and the resultant local dendritic and propagated somatic voltage response were recorded in the  $I_h(+)$  (blue) and the  $I_h(-)$  model (red). The locations of 18 separate synaptic inputs are shown in (C).  
 (E) The delay between the maximal amplitude of AMPA-like conductance and EPSPs peak recorded at the soma as a function of synaptic distance from soma in the  $I_h(+)$  (blue) and the  $I_h(-)$  model.  
 (F) Synaptic delays and half-width of the EPSPs calculated for  $I_h(+)$  and  $I_h(-)$  models.  
 (G) The integral of EPSPs recorded at the soma in response to bursts of synaptic input at various frequencies. The somatic response in the  $I_h(+)$  model was decreased relative to the  $I_h(-)$  model across several frequencies of synaptic input.  
 (H) Power spectrum of the somatic membrane potential of the  $I_h(+)$  and  $I_h(-)$  model when stimulated by 1000 synapses randomly located along the apical dendrite (as shown in C). Black stripes correspond to statistically significant differences in the power spectrum (2 sample Kolmogorov-Smirnov test;  $p < 0.01$ ). Inset: location of a subset (100 out of 1,000) synapses is shown. Data are presented as mean  $\pm$  SD.

(e.g., Figure 3) despite only subtle depth-dependent differences in h-channel related RNA expression (Figure 1). Differences in the expression of TRIP8b (the gene product of *PEX5L*) isoforms may contribute to the depth-dependent differences in  $I_h$ -related properties we observed (Lewis et al., 2009). However,  $I_h$  is unlikely to explain all of the depth-dependent differences in intrinsic properties we observed between mouse and human pyramidal neurons. Indeed, blocking h-channels did not eliminate differences in  $R_N$  between superficial and deep neurons in human cortex. Clearly other factors, including morphology and/or differential expression of conductances other than  $I_h$ , may contribute to the depth- and species-dependence we observed.

Our findings have a few limitations and caveats that are inherent to studying human brain tissue at this level of analysis. First, human physiology data were collected from tissue obtained from neurosurgical patients and thus may be influenced by neurological disease state. Notably, h-channels are implicated in epilepsy (Brennan et al., 2016; Jung et al., 2007; Shin et al., 2008), and, thus, our results may be influenced by neuropathology. Several factors, however, strengthen our conclusion that  $I_h$  prominently contributes to the membrane properties of human supragranular pyramidal neurons in the neurotypical condition. First, the tissue obtained for these experiments was distal to the focus of the seizures and did not express overt signs of pathology. Second, we found similarly prominent  $I_h$ -related properties in pyramidal neurons from tumor patients and in other cortical regions (Figure S3; Allen Cell Types Database, <http://celltypes.brain-map.org>; Deitcher et al., 2017; Ting et al., 2018). Finally, h-channel subunit RNA is abundant in pyramidal neurons in the supragranular layers of cortex in post-mortem tissue obtained from donor brains with no prior history of neurological disorders (Figure 1; Figure S1) (Zeng et al., 2012).

### Functional Implications

Deep L3 neurons possess the most prominent  $I_h$ -related membrane properties in the supragranular layers of human temporal cortex. Deep L3 also corresponds to the sub-lamina containing the largest supragranular pyramidal neurons with the largest total dendritic length (von Economo and Koskinas, 2007; Mohan et al., 2015). Because of their large size, these neurons may require specialized intrinsic mechanisms to ensure faithful propagation of signals along their dendritic arbor. Our modeling results suggest that h-channels may serve in this regard by counteracting capacitive filtering by the dendrite.

Our simulations also demonstrate that h-channels significantly affect the integrative properties of human supragranular pyramidal neurons in a similar manner to what has been reported in rodent cortical L5 or hippocampal CA1 pyramidal neurons (Dem-brow et al., 2015; Vaidya and Johnston, 2013; Williams and Stuart, 2000). Consistent with its role as a resonating conductance (Hutcheon and Yarom, 2000; Narayanan and Johnston, 2008), the presence of  $I_h$  resulted in an increase in power in the theta (and higher) frequency range (Figure 7H). The specific details of these effects will depend upon several factors, including total abundance, subcellular localization, and/or gradients of the channels. In rodents, h-channels are enriched in the distal apical dendrites of several types of pyramidal neurons in multiple brain regions (Harnett et al., 2015; Kalmbach et al., 2013; Kole et al.,

2006; Lörincz et al., 2002; Williams and Stuart, 2000). Notably, we observed widespread expression in human temporal cortex of a gene (*PEX5L*) that codes for TRIP8b, a protein that is necessary for dendritic enrichment of  $I_h$  (Lewis et al., 2009, 2011). Thus, our results are consistent with the possibility that  $I_h$  is prominent in the dendrites of human supragranular pyramidal neurons. Nevertheless, modeling studies suggest that the effects of  $I_h$  on EPSP kinetics do not appear to depend on subcellular gradients, but rather on total expression levels (Angelo et al., 2007; Das and Narayanan, 2014). Similarly, we observed that the selective transfer of synaptic input containing theta band frequencies was robust to different somatic-dendritic gradients of  $I_h$  (Figure S7).

Finally, our results suggest that  $I_h$  may significantly affect the spike initiation dynamics of human supragranular pyramidal neurons. The presence of h-channels can switch the firing mode of a neuron from temporal integrator to coincidence detector, whereby spiking is sensitive to correlated synaptic input rather than changes in mean presynaptic firing rate (Das and Narayanan, 2017, 2014; Ratté et al., 2013). For rodent neurons, there is an intimate relationship between sub- and suprathreshold spectral selectivity (Das and Narayanan, 2017, 2014). Thus, the spiking activity of human supragranular pyramidal neurons may be tuned to specific frequencies of synaptic input, and this selectivity may vary with somatic depth from the pial surface. If so, the expression of h-channels in supragranular pyramidal neurons may contribute to the dominant delta/theta band oscillations apparent in human supragranular cortex (Halgren et al., 2018) and to memory-related theta-frequency phase-locking of single human neurons observed *in vivo* (Jacobs et al., 2007; Rutishauser et al., 2010).

### STAR★METHODS

Detailed methods are provided in the online version of this paper and include the following:

- KEY RESOURCES TABLE
- CONTACT FOR REAGENT AND RESOURCE SHARING
- EXPERIMENTAL MODEL AND SUBJECT DETAILS
  - Human surgical specimens
  - Mouse specimens
- METHOD DETAILS
  - Acute brain slice preparation
  - Patch clamp recordings
  - Biophysical model
  - Single cell/nuclei sequencing
  - Multiplex fluorescence *in situ* hybridization (mFISH)
  - Image acquisition
- QUANTIFICATION AND STATISTICAL ANALYSIS
  - Physiology and modeling
  - mFISH
- DATA AND SOFTWARE AVAILABILITY

### SUPPLEMENTAL INFORMATION

Supplemental Information includes seven figures and two tables and can be found with this article online at <https://doi.org/10.1016/j.neuron.2018.10.012>.

## ACKNOWLEDGMENTS

We wish to thank the Allen Institute founder, Paul G. Allen, for his vision, encouragement, and support. Research reported in this publication was supported by the National Institute of Mental Health of the National Institutes of Health under award number U01MH114812, and the Chan Zuckerberg Initiative, an advised fund of Silicon Valley Community Foundation under award number 2017-174399. The content is solely the responsibility of the authors and does not necessarily represent the official views of the National Institutes of Health or the Chan Zuckerberg Initiative. We also wish to thank the Allen Institute for Brain Science Tissue Procurement, Tissue Processing, and Facilities teams for help in coordinating the logistics of human tissue surgical tissue collection, transport, and processing. We also thank the Allen Institute for Brain Science Reagent Preparation, Animal Care, and In Vitro Single Cell Characterization teams. We are grateful to our collaborators at the local hospital sites, including Tracie Granger, Caryl Tongco, Matt Ormond, Jae-Guen Yoon, Nathan Hansen, Niki Ellington, Rachel Iverson (Swedish Medical Center), Carolyn Bea, Gina DeNoble, and Allison Beller (Harborview Medical Center). We also thank Meanhwan Kim for helpful discussions and suggestions.

## AUTHOR CONTRIBUTIONS

Conceptualization, B.E.K., C.A.A., C.K., E.S.L., and J.T.T.; Methodology, B.E.K., J.T.T., A.B., A.N., K.D., C.A.A., B.L., J.C., and P.R.N.; Software, B.E.K., A.B., A.N., K.D., C.A.A., and B.L.; Validation, B.E.K., A.B., C.A.A., B.L., J.T.T.; Formal Analysis, B.E.K., A.B., B.L., J.A.M., and T.E.B.; Investigation, B.E.K., A.B., B.L., J.C., Z.M., P.C., J.T.T., R.D.H., and R.d.F.; Resources, C.D.K., D.L.S., R.P.G., C.C., A.L.K., and J.G.O.; Data Curation, B.E.K., A.B., B.L., J.A.M., T.E.B., and C.A.A.; Writing – Original Draft, B.E.K. and A.B.; Writing – Review & Editing, B.L., J.A.M., T.E.B., C.K., C.A.A., E.L., and J.T.T.; Visualization, B.E.K., A.B., J.A.M., J.C., and B.L.; Supervision, C.K., C.A.A., E.S.L., and J.T.T.; Project Administration, B.E.K., A.C.C., C.K., C.A.A., E.S.L., and J.T.T.; Funding Acquisition, E.S.L. and C.K.

## DECLARATION OF INTERESTS

The authors declare no competing interests.

Received: April 27, 2018

Revised: September 5, 2018

Accepted: October 5, 2018

Published: November 1, 2018

## REFERENCES

- Andrasfalvy, B.K., and Magee, J.C. (2001). Distance-dependent increase in AMPA receptor number in the dendrites of adult hippocampal CA1 pyramidal neurons. *J. Neurosci.* *21*, 9151–9159.
- Angelo, K., London, M., Christensen, S.R., and Häusser, M. (2007). Local and global effects of I(h) distribution in dendrites of mammalian neurons. *J. Neurosci.* *27*, 8643–8653.
- Angevine, J.B., Jr., and Sidman, R.L. (1961). Autoradiographic study of cell migration during histogenesis of cerebral cortex in the mouse. *Nature* *192*, 766–768.
- Bean, B.P. (2007). The action potential in mammalian central neurons. *Nat. Rev. Neurosci.* *8*, 451–465.
- Brennan, G.P., Baram, T.Z., and Poolos, N.P. (2016). Hyperpolarization-activated cyclic nucleotide-gated (HCN) channels in epilepsy. *Cold Spring Harb. Perspect. Med.* *6*, a022384.
- Campagnola, L., Kratz, M.B., and Manis, P.B. (2014). ACQ4: an open-source software platform for data acquisition and analysis in neurophysiology research. *Front. Neuroinform.* *8*, 3.
- Colantuoni, C., Lipska, B.K., Ye, T., Hyde, T.M., Tao, R., Leek, J.T., Colantuoni, E.A., Elkahloun, A.G., Herman, M.M., Weinberger, D.R., and Kleinman, J.E. (2011). Temporal dynamics and genetic control of transcription in the human prefrontal cortex. *Nature* *478*, 519–523.
- Das, A., and Narayanan, R. (2014). Active dendrites regulate spectral selectivity in location-dependent spike initiation dynamics of hippocampal model neurons. *J. Neurosci.* *34*, 1195–1211.
- Das, A., and Narayanan, R. (2017). Theta-frequency selectivity in the somatic spike-triggered average of rat hippocampal pyramidal neurons is dependent on HCN channels. *J. Neurophysiol.* *118*, 2251–2266.
- DeFelipe, J. (2011). The evolution of the brain, the human nature of cortical circuits, and intellectual creativity. *Front. Neuroanat.* *5*, 29.
- Deitcher, Y., Eyal, G., Kanari, L., Verhoog, M.B., Atenekeng Kahou, G.A., Mansvelder, H.D., de Kock, C.P.J., and Segev, I. (2017). Comprehensive morpho-electrotonic analysis shows 2 distinct classes of L2 and L3 pyramidal neurons in human temporal cortex. *Cereb. Cortex* *27*, 5398–5414.
- Dembrow, N.C., Chitwood, R.A., and Johnston, D. (2010). Projection-specific neuromodulation of medial prefrontal cortex neurons. *J. Neurosci.* *30*, 16922–16937.
- Dembrow, N.C., Zemelman, B.V., and Johnston, D. (2015). Temporal dynamics of L5 dendrites in medial prefrontal cortex regulate integration versus coincidence detection of afferent inputs. *J. Neurosci.* *35*, 4501–4514.
- Edelstein, A.D., Tsuchida, M.A., Amodaj, N., Pinkard, H., Vale, R.D., and Stuurman, N. (2014). Advanced methods of microscope control using  $\mu$ Manager software. *J. Biol. Methods* *7*, 10.
- Eyal, G., Mansvelder, H.D., de Kock, C.P.J., and Segev, I. (2014). Dendrites impact the encoding capabilities of the axon. *J. Neurosci.* *34*, 8063–8071.
- Eyal, G., Verhoog, M.B., Testa-Silva, G., Deitcher, Y., Lodder, J.C., Benavides-Piccione, R., Morales, J., DeFelipe, J., de Kock, C.P., Mansvelder, H.D., and Segev, I. (2016). Unique membrane properties and enhanced signal processing in human neocortical neurons. *eLife* *5*, 5.
- Fan, Y., Fricker, D., Brager, D.H., Chen, X., Lu, H.-C., Chitwood, R.A., and Johnston, D. (2005). Activity-dependent decrease of excitability in rat hippocampal neurons through increases in I(h). *Nat. Neurosci.* *8*, 1542–1551.
- Foehring, R.C., and Waters, R.S. (1991). Contributions of low-threshold calcium current and anomalous rectifier (Ih) to slow depolarizations underlying burst firing in human neocortical neurons in vitro. *Neurosci. Lett.* *124*, 17–21.
- Gao, Y., and Kilfoil, M.L. (2009). Accurate detection and complete tracking of large populations of features in three dimensions. *Opt. Express* *17*, 4685–4704.
- Golding, N.L., Mickus, T.J., Katz, Y., Kath, W.L., and Spruston, N. (2005). Factors mediating powerful voltage attenuation along CA1 pyramidal neuron dendrites. *J. Physiol.* *568*, 69–82.
- Gouwens, N.W., Berg, J., Feng, D., Sorensen, S.A., Zeng, H., Hawrylycz, M.J., Koch, C., and Arkhipov, A. (2018). Systematic generation of biophysically detailed models for diverse cortical neuron types. *Nat. Commun.* *9*, 710.
- Gratiy, S.L., Billeh, Y.N., Dai, K., Mitelut, C., Feng, D., Gouwens, N.W., Cain, N., Koch, C., Anastassiou, C.A., and Arkhipov, A. (2018). BioNet: a python interface to NEURON for modeling large-scale networks. *PLoS ONE* *13*, e0201630.
- Gu, N., Vervaeke, K., Hu, H., and Storm, J.F. (2005). Kv7/KCNQ/M and HCN/h, but not KCa2/SK channels, contribute to the somatic medium after-hyperpolarization and excitability control in CA1 hippocampal pyramidal cells. *J. Physiol.* *566*, 689–715.
- Halgren, M., Fabó, D., Ulbert, I., Madsen, J.R., Eröss, L., Doyle, W.K., Devinsky, O., Schomer, D., Cash, S.S., and Halgren, E. (2018). Superficial slow rhythms integrate cortical processing in humans. *Sci. Rep.* *8*, 2055.
- Harnett, M.T., Magee, J.C., and Williams, S.R. (2015). Distribution and function of HCN channels in the apical dendritic tuft of neocortical pyramidal neurons. *J. Neurosci.* *35*, 1024–1037.
- Hill, R.S., and Walsh, C.A. (2005). Molecular insights into human brain evolution. *Nature* *437*, 64–67.
- Hutcheon, B., and Yarom, Y. (2000). Resonance, oscillation and the intrinsic frequency preferences of neurons. *Trends Neurosci.* *23*, 216–222.
- Hutcheon, B., Miura, R.M., and Puil, E. (1996). Subthreshold membrane resonance in neocortical neurons. *J. Neurophysiol.* *76*, 683–697.

- Jacobs, J., Kahana, M.J., Ekstrom, A.D., and Fried, I. (2007). Brain oscillations control timing of single-neuron activity in humans. *J. Neurosci.* *27*, 3839–3844.
- Johnston, D., and Narayanan, R. (2008). Active dendrites: colorful wings of the mysterious butterflies. *Trends Neurosci.* *31*, 309–316.
- Jonas, P., and Sakmann, B. (1992). Glutamate receptor channels in isolated patches from CA1 and CA3 pyramidal cells of rat hippocampal slices. *J. Physiol.* *455*, 143–171.
- Jung, S., Jones, T.D., Lugo, J.N., Jr., Sheerin, A.H., Miller, J.W., D'Ambrosio, R., Anderson, A.E., and Poolos, N.P. (2007). Progressive dendritic HCN channelopathy during epileptogenesis in the rat pilocarpine model of epilepsy. *J. Neurosci.* *27*, 13012–13021.
- Kalmbach, B.E., Chitwood, R.A., Dembrow, N.C., and Johnston, D. (2013). Dendritic generation of mGluR-mediated slow afterdepolarization in layer 5 neurons of prefrontal cortex. *J. Neurosci.* *33*, 13518–13532.
- Kalmbach, B.E., Johnston, D., and Brager, D.H. (2015). Cell-type specific channelopathies in the prefrontal cortex of the *fmr1*<sup>-y</sup> mouse model of fragile X syndrome(1,2,3). *eNeuro* *2*.
- Kalmbach, B.E., Gray, R., Johnston, D., and Cook, E.P. (2017). Systems-based analysis of dendritic nonlinearities reveals temporal feature extraction in mouse L5 cortical neurons. *J. Neurophysiol.* *117*, 2188–2208.
- Koch, C. (1984). Cable theory in neurons with active, linearized membranes. *Biol. Cybern.* *50*, 15–33.
- Koch, C. (2004). *Biophysics of Computation* (Oxford University Press).
- Koch, C., Douglas, R., and Wehmeier, U. (1990). Visibility of synaptically induced conductance changes: theory and simulations of anatomically characterized cortical pyramidal cells. *J. Neurosci.* *10*, 1728–1744.
- Kole, M.H.P., Hallermann, S., and Stuart, G.J. (2006). Single Ih channels in pyramidal neuron dendrites: properties, distribution, and impact on action potential output. *J. Neurosci.* *26*, 1677–1687.
- Larkum, M.E., Waters, J., Sakmann, B., and Helmchen, F. (2007). Dendritic spikes in apical dendrites of neocortical layer 2/3 pyramidal neurons. *J. Neurosci.* *27*, 8999–9008.
- Lewis, A.S., Schwartz, E., Chan, C.S., Noam, Y., Shin, M., Wadman, W.J., Surmeier, D.J., Baram, T.Z., Macdonald, R.L., and Chetkovich, D.M. (2009). Alternatively spliced isoforms of TRIP8b differentially control h channel trafficking and function. *J. Neurosci.* *29*, 6250–6265.
- Lewis, A.S., Vaidya, S.P., Blaiss, C.A., Liu, Z., Stoub, T.R., Brager, D.H., Chen, X., Bender, R.A., Estep, C.M., Popov, A.B., et al. (2011). Deletion of the hyperpolarization-activated cyclic nucleotide-gated channel auxiliary subunit TRIP8b impairs hippocampal Ih localization and function and promotes antidepressant behavior in mice. *J. Neurosci.* *31*, 7424–7440.
- Lörincz, A., Notomi, T., Tamás, G., Shigemoto, R., and Nusser, Z. (2002). Polarized and compartment-dependent distribution of HCN1 in pyramidal cell dendrites. *Nat. Neurosci.* *5*, 1185–1193.
- Lyubimova, A., Itzkovitz, S., Junker, J.P., Fan, Z.P., Wu, X., and van Oudenaarden, A. (2013). Single-molecule mRNA detection and counting in mammalian tissue. *Nat. Protoc.* *8*, 1743–1758.
- Magee, J.C. (1998). Dendritic hyperpolarization-activated currents modify the integrative properties of hippocampal CA1 pyramidal neurons. *J. Neurosci.* *18*, 7613–7624.
- Magee, J.C. (1999). Dendritic Ih normalizes temporal summation in hippocampal CA1 neurons. *Nat. Neurosci.* *2*, 848.
- Mauro, A. (1961). Anomalous impedance, a phenomenological property of time-variant resistance. An analytic review. *Biophys. J.* *1*, 353–372.
- Mohan, H., Verhoog, M.B., Doreswamy, K.K., Eyal, G., Aardse, R., Lodder, B.N., Goriounova, N.A., Asamoah, B., Brakspear, A.B., Groot, C., et al. (2015). Dendritic and axonal architecture of individual pyramidal neurons across layers of adult human neocortex. *Cereb. Cortex* *25*, 4839–4853.
- Molnár, Z., Kaas, J.H., de Carlos, J.A., Hevner, R.F., Lein, E., and Némec, P. (2014). Evolution and development of the mammalian cerebral cortex. *Brain Behav. Evol.* *83*, 126–139.
- Narayanan, R., and Johnston, D. (2007). Long-term potentiation in rat hippocampal neurons is accompanied by spatially widespread changes in intrinsic oscillatory dynamics and excitability. *Neuron* *56*, 1061–1075.
- Narayanan, R., and Johnston, D. (2008). The h channel mediates location dependence and plasticity of intrinsic phase response in rat hippocampal neurons. *J. Neurosci.* *28*, 5846–5860.
- Nolan, M.F., Malleret, G., Dudman, J.T., Buhl, D.L., Santoro, B., Gibbs, E., Vronskaya, S., Buzsáki, G., Siegelbaum, S.A., Kandel, E.R., and Morozov, A. (2004). A behavioral role for dendritic integration: HCN1 channels constrain spatial memory and plasticity at inputs to distal dendrites of CA1 pyramidal neurons. *Cell* *119*, 719–732.
- Peng, H., Ruan, Z., Long, F., Simpson, J.H., and Myers, E.W. (2010). V3D enables real-time 3D visualization and quantitative analysis of large-scale biological image data sets. *Nat. Biotechnol.* *28*, 348–353.
- Rakic, P. (1974). Neurons in rhesus monkey visual cortex: systematic relation between time of origin and eventual disposition. *Science* *183*, 425–427.
- Rakic, P. (2009). Evolution of the neocortex: a perspective from developmental biology. *Nat. Rev. Neurosci.* *10*, 724–735.
- Rall, W. (1967). Distinguishing theoretical synaptic potentials computed for different soma-dendritic distributions of synaptic input. *J. Neurophysiol.* *30*, 1138–1168.
- Ratté, S., Hong, S., De Schutter, E., and Prescott, S.A. (2013). Impact of neuronal properties on network coding: roles of spike initiation dynamics and robust synchrony transfer. *Neuron* *78*, 758–772.
- Robinson, R.B., and Siegelbaum, S.A. (2003). Hyperpolarization-activated cation currents: from molecules to physiological function. *Annu. Rev. Physiol.* *65*, 453–480.
- Rothman, J.S., and Silver, R.A. (2018). NeuroMatic: an integrated open-source software toolkit for acquisition, analysis and simulation of electrophysiological data. *Front. Neuroinform.* *12*, 14.
- Routh, B.N., Rathour, R.K., Baumgardner, M.E., Kalmbach, B.E., Johnston, D., and Brager, D.H. (2017). Increased transient Na<sup>+</sup> conductance and action potential output in layer 2/3 prefrontal cortex neurons of the *fmr1*<sup>-y</sup> mouse. *J. Physiol.* *595*, 4431–4448.
- Rueden, C.T., Schindelin, J., Hiner, M.C., DeZonia, B.E., Walter, A.E., Arena, E.T., and Eliceiri, K.W. (2017). ImageJ2: ImageJ for the next generation of scientific image data. *BMC Bioinformatics* *18*, 529.
- Rutishauser, U., Ross, I.B., Mamelak, A.N., and Schuman, E.M. (2010). Human memory strength is predicted by theta-frequency phase-locking of single neurons. *Nature* *464*, 903–907.
- Santoro, B., Chen, S., Luthi, A., Pavlidis, P., Shumyatsky, G.P., Tibbs, G.R., and Siegelbaum, S.A. (2000). Molecular and functional heterogeneity of hyperpolarization-activated pacemaker channels in the mouse CNS. *J. Neurosci.* *20*, 5264–5275.
- Santoro, B., Wainger, B.J., and Siegelbaum, S.A. (2004). Regulation of HCN channel surface expression by a novel C-terminal protein-protein interaction. *J. Neurosci.* *24*, 10750–10762.
- Schindelin, J., Arganda-Carreras, I., Frise, E., Kaynig, V., Longair, M., Pietzsch, T., Preibisch, S., Rueden, C., Saalfeld, S., Schmid, B., et al. (2012). Fiji: an open-source platform for biological-image analysis. *Nat. Methods* *9*, 676–682.
- Shin, M., Brager, D., Jaramillo, T.C., Johnston, D., and Chetkovich, D.M. (2008). Mislocalization of h channel subunits underlies h channelopathy in temporal lobe epilepsy. *Neurobiol. Dis.* *32*, 26–36.
- Spruston, N., Jonas, P., and Sakmann, B. (1995). Dendritic glutamate receptor channels in rat hippocampal CA3 and CA1 pyramidal neurons. *J. Physiol.* *482*, 325–352.
- Stuart, G., and Spruston, N. (1998). Determinants of voltage attenuation in neocortical pyramidal neuron dendrites. *J. Neurosci.* *18*, 3501–3510.
- Stuart, G.J., and Spruston, N. (2015). Dendritic integration: 60 years of progress. *Nat. Neurosci.* *18*, 1713–1721.
- Tasic, B., Menon, V., Nguyen, T.N., Kim, T.K., Jarsky, T., Yao, Z., Levi, B., Gray, L.T., Sorensen, S.A., Dolbeare, T., et al. (2016). Adult mouse cortical

- cell taxonomy revealed by single cell transcriptomics. *Nat. Neurosci.* **19**, 335–346.
- Testa-Silva, G. (2010). Human Synapses Show a Wide Temporal Window for Spike-Timing-Dependent Plasticity (*Front. Syn. Neurosci.*).
- Testa-Silva, G., Verhoog, M.B., Linaro, D., de Kock, C.P.J., Baayen, J.C., Meredith, R.M., De Zeeuw, C.I., Giugliano, M., and Mansvelde, H.D. (2014). High bandwidth synaptic communication and frequency tracking in human neocortex. *PLoS Biol.* **12**, e1002007.
- Ting, J.T., Daigle, T.L., Chen, Q., and Feng, G. (2014). Acute brain slice methods for adult and aging animals: application of targeted patch clamp analysis and optogenetics. In *Methods in Molecular Biology*, J.M. Walker, ed. (Springer New York), pp. 221–242.
- Ting, J.T., Kalmbach, B., Chong, P., Frates, R., Keene, C.D., Gwinn, R.P., Cobbs, C., Ko, A.L., Ojemann, J.G., Ellenbogen, R.G., et al. (2018). Experimental platform for molecular-genetic dissection of adult human neocortical cell types and circuits. *Sci. Rep.* **8**, 8407.
- Ulrich, D. (2002). Dendritic resonance in rat neocortical pyramidal cells. *J. Neurophysiol.* **87**, 2753–2759.
- Vaidya, S.P., and Johnston, D. (2013). Temporal synchrony and gamma-to-theta power conversion in the dendrites of CA1 pyramidal neurons. *Nat. Neurosci.* **16**, 1812–1820.
- van Aerde, K.I., and Feldmeyer, D. (2015). Morphological and physiological characterization of pyramidal neuron subtypes in rat medial prefrontal cortex. *Cereb. Cortex* **25**, 788–805.
- Van Geit, W., Gevaert, M., Chindemi, G., Rössert, C., Courcol, J.D., Muller, E.B., Schürmann, F., Segev, I., and Markram, H. (2016). BluePyOpt: leveraging open source software and cloud infrastructure to optimise model parameters in neuroscience. *Front. Neuroinform.* **10**, 17.
- von Economo, C.F., and Koskinas, G.N. (2007). *Atlas of Cytoarchitectonics of the Adult Human Cerebral Cortex* (S. Karger AG).
- Wang, B., Yin, L., Zou, X., Ye, M., Liu, Y., He, T., Deng, S., Jiang, Y., Zheng, R., Wang, Y., et al. (2015). A subtype of inhibitory interneuron with intrinsic persistent activity in human and monkey neocortex. *Cell Rep.* **10**, 1450–1458.
- Williams, S.R., and Stuart, G.J. (2000). Site independence of EPSP time course is mediated by dendritic I(h) in neocortical pyramidal neurons. *J. Neurophysiol.* **83**, 3177–3182.
- Zeng, H., Shen, E.H., Hohmann, J.G., Oh, S.W., Bernard, A., Royall, J.J., Glattfelder, K.J., Sunkin, S.M., Morris, J.A., Guillozet-Bongaarts, A.L., et al. (2012). Large-scale cellular-resolution gene profiling in human neocortex reveals species-specific molecular signatures. *Cell* **149**, 483–496.

## STAR★METHODS

## KEY RESOURCES TABLE

REAGENT or RESOURCE	SOURCE	IDENTIFIER
Chemicals, Peptides, and Recombinant Proteins		
ZD7288	Tocris	Cat#1000; CAS: 13305
20XSSC	Sigma Aldrich	Cat#S6639
SDS	Sigma Aldrich	Cat#L3771
Boric acid	Sigma Aldrich	Cat#B6768
TE pH 8	Sigma Aldrich	Cat#8890-OP
Formamide	Sigma Aldrich	Cat#F9037
Dextran Sulfate	Sigma Aldrich	Cat#D8906
BSA	Ambion	Cat#AM2616
Ribonucleoside vanadyl complex	New England Biolabs	Cat#S1402S
tRNA	Sigma Aldrich	Cat#10109541001
DAPI	Sigma Aldrich	Cat#32670
Glucose Oxidase	Sigma Aldrich	Cat#G2133
Catalase	Sigma Aldrich	Cat#C3515
Deposited Data		
Allen Cell Types Database	Allen Institute for Brain Science	<a href="http://celltypes.brain-map.org/">http://celltypes.brain-map.org/</a>
Allen Brain Atlas	Allen Institute for Brain Science	<a href="http://human.brain-map.org/">http://human.brain-map.org/</a> ; <a href="http://mouse.brain-map.org/">http://mouse.brain-map.org/</a>
Experimental Models: Organisms/Strains		
Mouse: C57BL/6-Tg(Pvalb-tdTomato)15Gfng/J	The Jackson Laboratory	JAX:027395
Mouse: Gad2-IRES-Cre	The Jackson Laboratory	JAX:010802
Mouse: Ndnf-IRES-Cre	The Jackson Laboratory	JAX:028536
Mouse: Slc32a-IRES-Cre	The Jackson Laboratory	JAX:028862
Vip-IRES-Cre	The Jackson Laboratory	JAX:010908
Slc17a6-IRES-Cre	The Jackson Laboratory	JAX:016963
Chat_IRES-Cre-neo	The Jackson Laboratory	JAX:006410
Sst-IRES-Cre	The Jackson Laboratory	JAX:013044
Oligonucleotides		
Probes for mFISH, See <a href="#">Table S2</a>	This paper	N/A
Software and Algorithms		
Igor Pro	Wavemetrics	RRID: SCR_000325; <a href="https://www.wavemetrics.com/products/igorpro">https://www.wavemetrics.com/products/igorpro</a>
GraphPad Prism	GraphPad	RRID: SCR_002798; <a href="https://www.graphpad.com/">https://www.graphpad.com/</a>
NeuroMatic	NeuroMatic	RRID: SCR_03577; <a href="http://www.neuromatic.thinkrandom.com/">http://www.neuromatic.thinkrandom.com/</a>
Vaa3d	Allen Institute for Brain Science	RRID: SCR_002609; <a href="http://www.alleninstitute.org/what-we-do/brain-science/research/products-tools/vaa3d/">http://www.alleninstitute.org/what-we-do/brain-science/research/products-tools/vaa3d/</a>
Neuron 7.4	Github	RRID: SCR_005984; <a href="https://github.com/AllenInstitute/bmtk">https://github.com/AllenInstitute/bmtk</a>
DEAP library	Github	<a href="https://github.com/DEAP/deap">https://github.com/DEAP/deap</a>
ACQ4	Acq4.org	<a href="http://Acq4.org">Acq4.org</a>
Micromanager	Micromanager.org	RRID: SCR_000415; <a href="http://micromanager.org">http://micromanager.org</a>
Fiji	GPL v2, Fiji	<a href="http://fiji.sc/Fiji">http://fiji.sc/Fiji</a>
PClump 10	Molecular Devices	RRID: SCR_011323; <a href="http://www.moleculardevices.com/products/software/pclump.html">http://www.moleculardevices.com/products/software/pclump.html</a>

## CONTACT FOR REAGENT AND RESOURCE SHARING

Further information and requests for resources and reagents should be directed to Brian Kalmbach ([briank@alleninstitute.org](mailto:briank@alleninstitute.org)).

## EXPERIMENTAL MODEL AND SUBJECT DETAILS

### Human surgical specimens

Surgical specimens were obtained from local hospitals (Harborview Medical Center, Swedish Medical Center and University of Washington Medical Center) in collaboration with local neurosurgeons. All patients provided informed consent and experimental procedures were approved by hospital institute review boards before commencing the study. The bulk of data included in this study were obtained from tissue from 12 patients with temporal lobe epilepsy with a mean age of  $37.85 \pm 4.29$ . Five patients were male and 7 were female. Additionally, data were obtained from tissue from five patients who had undergone deep tumor resection from the temporal lobe (one male and two female) or frontal cortex (one male and one female). Additional patient information can be found in [Table S1](#).

### Mouse specimens

All procedures involving mice were approved by the Institutional Animal Care and Use Committee of the Allen Institute for Brain Science. Mixed strains of transgenic mice (5 male and 8 female mice), from 44–61 days old (mean =  $51.08 \pm 5.45$  days old) were used for experiments. Strains of mice used in this study included: C57BL/6-Tg(Pvalb-tdTomato)15Gfng/J, Gad2-IRES-Cre, Ndnf-IRES-Cre, Slc32a-IRES-Cre, Vip-IRES-Cre, Slc17a6-IRES-Cre, Chat\_IRES-Cre-neo, and Sst-IRES-Cre. All animals were housed 3–5 per cage and maintained on a 12-hour light/dark cycle in a temperature and humidity controlled room with freely accessible water and food.

## METHOD DETAILS

### Acute brain slice preparation

Tissue obtained from surgery was distal to the core pathological tissue and was deemed not to be of diagnostic value. Specimens were placed in a sterile container filled with an artificial cerebral spinal fluid (aCSF) composed of (in mM): 92 with N-methyl-D-glucamine (NMDG), 2.5 KCl, 1.25  $\text{NaH}_2\text{PO}_4$ , 30  $\text{NaHCO}_3$ , 20 4-(2-hydroxyethyl)-1-piperazineethanesulfonic acid (HEPES), 25 glucose, 2 thiourea, 5 Na-ascorbate, 3 Na-pyruvate, 0.5  $\text{CaCl}_2 \cdot 4\text{H}_2\text{O}$  and 10  $\text{MgSO}_4 \cdot 7\text{H}_2\text{O}$ . The pH of the NMDG aCSF was titrated to pH 7.3–7.4 with concentrated hydrochloric acid and the osmolality was 300–305 mOsmoles/Kg. The solution was pre-chilled to 2–4°C and thoroughly bubbled with carbogen (95%  $\text{O}_2$ /5%  $\text{CO}_2$ ) prior to collection. Surgical specimens were quickly transported from the surgical site to the laboratory while continuously bubbled with carbogen (transportation time: 10–40 minutes).

To ensure that the dendrites of pyramidal neurons were relatively intact, human surgical specimens were trimmed and mounted such that the angle of slicing was perpendicular to the pial surface. 350  $\mu\text{m}$  thick slices were sectioned on a Compressome VF-200 (Precisionary Instruments) using the NMDG protective recovery method ([Ting et al., 2014](#)) and either a zirconium ceramic blade (EF-INZ10, Cadence) or a sapphire knife (93060, Electron Microscopy Sciences). The slicing solution was the same as used for transport from the hospital to the laboratory. After all sections were obtained, slices were transferred to a warmed (32–34°C) initial recovery chamber filled with NMDG aCSF under constant carbogenation. After 12 minutes, slices were transferred to a Brain Slice Keeper-4 holding chamber (Automate Scientific) containing an aCSF solution made of (in mM): 92 NaCl, 2.5 KCl, 1.25  $\text{NaH}_2\text{PO}_4$ , 30  $\text{NaHCO}_3$ , 20 HEPES, 25 glucose, 2 thiourea, 5 Na-ascorbate, 3 Na-pyruvate, 2  $\text{CaCl}_2 \cdot 4\text{H}_2\text{O}$  and 2  $\text{MgSO}_4 \cdot 7\text{H}_2\text{O}$  continuously bubbled with 95/5  $\text{O}_2/\text{CO}_2$ . Slices were held in this chamber at room temperature for 1–48 hours before transfer to the recording chamber for patch clamp recording.

Mice were deeply anesthetized by intraperitoneal administration of Avertin (20 mg/kg IP) and were perfused through the heart with NMDG aCSF (bubbled with carbogen). Coronal slices containing the temporal association area (TeA) were prepared as described for human with the exception that slices were 300  $\mu\text{m}$  rather than 350  $\mu\text{m}$  thick.

### Patch clamp recordings

Slices were placed in a submerged, heated (32–34°C) recording chamber that was continually perfused (3–4 mL/min) with aCSF under constant carbogenation and containing the following (in mM): 119 NaCl, 2.5 KCl, 1.25  $\text{NaH}_2\text{PO}_4$ , 24  $\text{NaHCO}_3$ , 12.5 glucose, 2  $\text{CaCl}_2 \cdot 4\text{H}_2\text{O}$  and 2  $\text{MgSO}_4 \cdot 7\text{H}_2\text{O}$  (pH 7.3–7.4). Slices were viewed with an Olympus BX51WI microscope and infrared differential interference contrast optics and a 40x water immersion objective. Patch pipettes (3–6 M $\Omega$ ) were pulled from borosilicate glass using a horizontal pipette puller (P1000, Sutter Instruments). The pipette solution for all experiments contained the following (in mM): 130 K-gluconate, 10 HEPES, 0.3 EGTA, 4 Mg-ATP, 0.3  $\text{Na}_2\text{-GTP}$  and 2  $\text{MgCl}_2$ . The pipette solution also contained 0.5% biocytin and 20  $\mu\text{M}$  Alexa 594. These were included to ensure that the apical dendrite reached the pial surface. Alexa filled cells were visualized only upon termination of the recording using a 540/605 nm excitation/emission filter set. The theoretical liquid junction potential was calculated to be –13 mV and was not corrected.

Whole cell somatic recordings were acquired using a Multiclamp 700B amplifier and PClamp 10 data acquisition software (Molecular Devices). Electrical signals were digitized (Axon Digidata 1550B) at 20–50 kHz and filtered at 2–10 kHz. Upon attaining whole-cell current clamp mode, the pipette capacitance was compensated and the bridge was balanced. Access resistance was monitored throughout the recording and was 8–25 M $\Omega$ . Recordings were terminated if access resistance exceeded 25 M $\Omega$ . ZD7288 (10  $\mu$ M; Tocris) was prepared from frozen concentrated stock solutions and diluted in recording aCSF.

### Biophysical model

The morphological reconstruction (Figure 7) was generated using methods previously described (Gouwens et al., 2018). Briefly, the tissue slice was stained via diaminobenzidine reaction to elucidate biocytin filled cells. Z stacks of the cell were imaged at 63x magnification on a Zeiss Axio Imager 2. Reconstruction was manually performed using Vaa3D software to create accurate full neuron representations of the soma, dendrites, and axon saved in the SWC format (Peng et al., 2010).

The single neuron model was simulated using the Neuron 7.4 simulator (<https://www.neuron.yale.edu/neuron/>) in combination with the Brain Modeling Toolkit (<https://github.com/AllenInstitute/bmtk>; Gratiy et al., 2018). The morphology of the simulated neuron was adopted from the SWC file generated in the morphology reconstruction process. The dendritic tree was discretized using 20  $\mu$ m spatial steps and corresponding cylindrical compartments were generated for all compartments. The model was simulated using temporal steps of 0.1 ms. We insured that further reduction of spatial and temporal discretization steps did not provide quantitatively different results. Leak conductance, capacitance, leak reversal potential and axial resistance were fitted to the subthreshold responses of a human pyramidal neuron with h-channels unblocked in response to the family of somatic current injections used to estimate passive parameters using genetic algorithms from DEAP library (<https://github.com/DEAP/deap>) and BluePyOpt (<https://github.com/BlueBrain/BluePyOpt>, Van Geit et al., 2016). To account for the surface area of spines we used the spine correction factor of 1.9 as in Eyal et al., 2016. Passive properties of single neurons can be substantially different in different parts of the cell (e.g., Golding et al., 2005, Stuart and Spruston 1998). As such, for the majority of simulations we chose not to constrain the passive parameters to a single value for the somatic, apical, basal and axonic compartments. For simulations in which passive parameters were allowed to vary depending upon subcellular compartment, the best parameters to fit the subthreshold responses were:  $g_{pas}^{soma} = 1 * 10^{-5} S/cm^2$ ;  $g_{pas}^{basal} = 2.34 * 10^{-6} S/cm^2$ ;  $g_{pas}^{axon} = 21 * 10^{-5} S/cm^2$ ;  $g_{pas}^{apical} = 15 * 10^{-5} S/cm^2$ ;  $g_{pas}^{soma} = 1 * 10^{-5} S/cm^2$ ;  $V_{leak}^{soma} = -79.65 mV$ ;  $V_{leak}^{basal} = -86.67 mV$ ;  $V_{leak}^{axon} = -68.35 mV$ ;  $V_{leak}^{apical} = -84.54 mV$ ;  $C_m^{soma} = 1.43 \mu F/cm^2$ ;  $C_m^{basal} = 0.95 \mu F/cm^2$ ;  $C_m^{axon} = 0.92 \mu F/cm^2$ ;  $C_m^{apic} = 1.45 \mu F/cm^2$ ;  $R_{axial}^{soma} = 577.6 Ohm * cm$ ;  $R_{axial}^{basal} = 197.75 Ohm * cm$ ;  $R_{axial}^{axon} = 630.19 Ohm * cm$ ;  $R_{axial}^{apical} = 747.71 Ohm * cm$ . For simulations in which passive parameters were set equally in all compartments, the best parameters to fit the subthreshold responses were:  $R_{axial} = 350.24 Ohm * cm$ ,  $C_m = 1.16 \mu F/cm^2$ ,  $E_{pas} = -86.97 mV$ ,  $g_{pas} = 6.60 * 10^{-6} S/cm^2$ . The kinetic parameters of  $I_h$  were adopted from Kole et al. (2006) and  $m_{\alpha}$  function was shifted by  $-20 mV$  to match the junction potential estimation from the experimental data. For most simulations  $I_h$  and the corresponding HCN conductance was uniformly distributed in somatic, axonal and dendritic compartments,  $g_{HCN} = 0.01 * 10^{-3} S/cm^2$ . We also tested the effects of different distributions of h-channels along the apical dendrite. We tested three additional gradients of  $I_h$ : 1) soma enriched, in which the apical dendrite ( $g_{HCN} = 0.005 * 10^{-3} S/cm^2$ ) had 50% less h-channel density than the soma ( $g_{HCN} = 0.01 * 10^{-3} S/cm^2$ ), 2) linearly increasing ( $g_{HCN} = (3.427e - 07) * (1.217 + 0.007 * distance)$ ), and 3) exponentially increasing ( $g_{HCN} = (2.849e - 07) * (-0.869 + 2.087 * \exp(0.003 * distance))$ ). The numerical coefficients for the linear and exponential approximations qualitatively matched the data from Harnett et al., 2015. The maximal conductance ( $g_{HCN}$ ) for  $I_h$  was adjusted such that the difference in  $R_N$  between the  $I_h(+)$  and  $I_h(-)$  models matched the difference in  $R_N$  observed in experiments after the blockade of  $I_h$  current by ZD7288. The model possessed no other active conductances. The model code is available on github page [https://github.com/AllenInstitute/human\\_neuron\\_Ih](https://github.com/AllenInstitute/human_neuron_Ih).

Synaptic conductances (10 nS) were simulated using AMPA-like kinetics:  $\tau_{rise} = 1.5 ms$ ,  $\tau_{decay} = 3 ms$ , reversal potential = 0 mV (Andrasfalvy and Magee, 2001; Jonas and Sakmann, 1992; Spruston et al., 1995). For simulations involving random activation of 1000 synaptic inputs, the synaptic conductance of each synapse was scaled to 0.001 mS/cm<sup>2</sup>. Three random seeds were instantiated using Python Numpy to generate temporal permutations of synaptic population activation (total simulation duration: 30 s). All results of simulations were stored in NWB file format (<https://www.nwb.org/>). Synapses were activated by a Poisson process with 4 Hz rate generated using Numpy expovariate() function. All simulations were performed on a MacBook Pro Retina with 2.8 GHz Intel core i7processor with 16 GB DDR3 RAM running Mac OS 10.13.3 Sierra.

### Single cell/nuclei sequencing

Detailed methods can be found at <http://celltypes.brain-map.org>. Briefly, for human tissue this method involved layer dissections of thin Nissl-stained human temporal cortex section, neuronal nuclei staining (NeuN) and Fluorescence-activated cells sorting (FACS) isolation, followed by Smart-seq v4 based library preparation and single-cell deep (2.5 million reads/cell) RNA-Seq. *GAD1* and *SLC17A7* expression were used to delineate inhibitory and excitatory neurons, respectively. Violin plots represent distribution of mRNA expression on a log scale with a maximum RPKM value of 400 for mouse and 4000 for human cells.

### Multiplex fluorescence in situ hybridization (mFISH)

10  $\mu$ m sections of fresh-frozen human MTG or mouse TeA tissue were prepared on Poly-L-lysine coated coverslips (as treated previously, Lyubimova et al., 2013), dried for 5–10 min at room temperature, then fixed with 4% PFA at 4 C for 15 min. Sections

were washed 3 × 10 min in PBS, permeabilized and dehydrated with 100% isopropanol at room temperature for 3 min, and allowed to dry. Sections were stored after isopropanol treatment at −80 C until use. Sections were rehydrated for 5 min in 2XSSC (Sigma Aldrich 20XSSC, 15557036), then treated 2 X 5 min with 4% SDS (Sigma Aldrich, 724255) and 200 mM boric acid (Sigma Aldrich, cat# B6768) pH 8.5 at room temperature. Sections were washed 3 times in 2X SSC, then once in TE pH 8 (Sigma Aldrich, 93283). Sections were heat-shocked at 70 C for 10 min in TE pH 8, followed by 2XSSC wash at room temperature. Sections were incubated in hybridization buffer (10% Formamide (v/v, Sigma Aldrich 4650), 10% Dextran Sulfate (w/v, Sigma Aldrich D8906), 200 μg/mL BSA (Ambion AM2616), 2 mM Ribonucleoside vanadyl complex (New England Biolabs, S1402S), 1mg/mL tRNA (Sigma 10109541001) in 2XSSC) for 5 min at 38.5 C. Probes were designed antisense to the following genes: *HCN1*, *HCN2*, *HCN3*, *HCN4*, *SLC17A7*, *GAD2* and *PEXL5* (Table S2). Probes were diluted to 250 nM in hybridization buffer and hybridized at 38.5 C for 2 h. Following hybridization, sections were washed 2 X 15 min at 38.5 C in wash buffer (2XSSC, 20% Formamide), and 1 X 15 min in wash buffer with 5 μg/mL DAPI (Sigma Aldrich, 32670). Sections are then imaged in Imaging buffer (20 mM Tris-HCl pH 8, 50 mM NaCl, 0.8% Glucose (Sigma Aldrich, G8270), 3 U/mL Glucose Oxidase (Sigma Aldrich, G2133), 90 U/mL Catalase (Sigma Aldrich, C3515). Following imaging, sections were incubated 3 X 10 min in stripping buffer (65% Formamide, 2X SSC) at 30 C to remove hybridization probes from the previous round. Sections are then washed in 2X SSC for 3 X 5 min at room temperature and the hybridization procedure was repeated.

### Image acquisition

mFISH images were collected using an inverted microscope in an epifluorescence configuration (Zeiss Axio Observer.Z1) with a 63x oil immersion objective with numerical aperture 1.4. Uniform excitation from one of four lasers (405, 488, 561 and 640 nm wavelengths) was achieved by imaging the front face of a square fiber after despeckling (Andor Borealis) and reflection off a quad-band dichroic. The sample was positioned in x,y and z with a motorized x,y stage with linear encoders and z piezo top-plate (Applied Scientific Instruments MS 2000-500) and z stacks with 300 nm plane spacing were collected in each color at each stage position. The z stacks were collected to include the entire z depth of the sample, typically about 35 planes. The fluorescence emission was filtered using a high-speed filterwheel (Zeiss) directly below the dichroic turret and imaged onto a sCMOS camera (Hamamatsu ORCA Flash4.0) with a final pixel size of 100 nm. Typical acquisition rates were ~30 s per location for 4-color z stacks at each x,y tile location. Images were collected after each round of hybridization using the same configuration of x,y tile locations, aligned manually before each acquisition based on DAPI fluorescence. The microscope was controlled using custom software built around ACQ4 (Campagnola et al., 2014) and using instrument drivers from Micro-manager (Edelstein et al., 2014).

## QUANTIFICATION AND STATISTICAL ANALYSIS

### Physiology and modeling

Data were analyzed using custom analysis scripts written in Igor Pro (Wavemetrics). ABF files were imported into Igor Pro using NeuroMatic (Rothman and Silver, 2018). All measurements were made at resting membrane potential and, in a subset of experiments, at a common potential of  $-65 \text{ mV} \pm 1 \text{ mV}$ . Input resistance ( $R_N$ ) was calculated from the linear portion of the current–voltage relationship generated in response to a series of 1 s current injections (−150 to +50 pA, 20 or 50 pA steps). The maximum and steady state voltage deflections were used to determine the maximum and steady state of  $R_N$ , respectively. Voltage sag was defined as the ratio of maximum to steady-state  $R_N$ . Rebound slope was calculated from the slope of the rebound amplitude as a function of steady-state membrane potential. Resonance was determined from the voltage response to a constant amplitude sinusoidal current injection that linearly increased in frequency from 1–14 or 15 Hz over 15 s. The impedance amplitude profile (ZAP) was constructed from the ratio of the fast Fourier transform of the voltage response to the fast Fourier transform of the current injection. The frequency corresponding to the peak impedance ( $Z_{\text{max}}$ ) was defined as the resonant frequency. The 3 dB cutoff was calculated as the frequency at which the ZAP profile attenuated to a value of  $(\sqrt{1/2}) Z_{\text{max}}$ . Action potentials (APs) were elicited in response to increasing amplitude, 1 s direct current injections (50–750 pA, 50 pA steps).

Statistical analyses and plotting were performed using Prism (Graphpad) or R. Data are presented in the text as mean ± SEM or  $R^2$  values. For physiology  $n$  = number of cells recorded (details in text or figure legends). Between-subject ANOVA, mixed factors ANOVA, two-sample Kolmogorov-Smirnov test and post hoc  $t$  tests were used to test for statistical differences between groups. Bonferroni correction was used to correct for multiple comparisons. Pearson's product moment correlation or Spearman correlation was used to test for statistically significant correlations between variables. ANCOVA was used to test for differences in linear fits.  $\alpha = 0.05$  or  $0.05/\text{number of comparisons}$ . Details of statistical comparisons can be found in the text or figure legends.

### mFISH

mFISH signal was observed as diffraction-limited spots which were localized in 3D image stacks by finding local maxima after spatial bandpass filtering, following Gao and Kilfoil (2009). These maxima were filtered for total intensity and radius to eliminate dim background and (in human tissue) large, bright lipofuscin granules. Further lipofuscin rejection was accomplished by eliminating particles detected as lipofuscin in another channel within one pixel or if a particle was detected in all fluorescence channels within two pixels of each detected particle.

Image tiles were stitched in the first round based of each acquisition on x,y stage position and then corresponding image tiles from subsequent rounds were registered to the first round using discrete Fourier transform-based image registration (<http://imreg-dft>).

[readthedocs.io/en/latest/index.html](http://readthedocs.io/en/latest/index.html)). The substrate for the registration was maximum intensity projections over z of bandpass filtered images of the 488 channel, utilizing lipofuscin fluorescence for registration. After registration, *GAD2*, *SLC17A7* and DAPI images were fused and down-sampled by two for manual segmentation and layer annotation.

Outlines of cells and cortical layers were manually annotated on images of *GAD2*, *SLC17A7* and DAPI as 2D polygons using the FIJI distribution (Schindelin et al., 2012) of ImageJ (Rueden et al., 2017). A single line was annotated along the cortical column used as the cortical depth axis.

Following localization of mFISH spots for all gene targets in each image tile, the locations in overlapping regions were duplicated and remaining spots within the 2D (xy) boundary of each cell outline were assigned to that cell. Membership in cortical layers was similarly assigned to each cell and the cortical depth coordinate was calculated as the projection of the x,y position onto the manually annotated cortical column axis. The resulting table of cells includes transcriptional profiles, layer membership and cortical depth.

### DATA AND SOFTWARE AVAILABILITY

Transcriptomic data are available at <http://celltypes.brain-map.org>.

ISH data are available at <http://human.brain-map.org>.